© 2018. Published by The Company of Biologists Ltd | Development (2018) 145, dev161182. doi:10.1242/dev.161182

RESEARCH ARTICLE

Defective endothelial cell migration in the absence of Cdc42 leads to capillary-venous malformations

Bàrbara Laviña[1], Marco Castro[1], Colin Niaudet[1], Bert Cruys[2,3], Alberto Álvarez-Aznar[1], Peter Carmeliet[2,3], Katie Bentley[1,4], Cord Brakebusch[5], Christer Betsholtz[1,6,*] and Konstantin Gaengel[1,*]

ABSTRACT

Formation and homeostasis of the vascular system requires several coordinated cellular functions, but their precise interplay during development and their relative importance for vascular pathologies remain poorly understood. Here, we investigated the endothelial functions regulated by Cdc42 and their *in vivo* relevance during angiogenic sprouting and vascular morphogenesis in the postnatal mouse retina. We found that Cdc42 is required for endothelial tip cell selection, directed cell migration and filopodia formation, but dispensable for cell proliferation or apoptosis. Although the loss of Cdc42 seems generally compatible with apical-basal polarization and lumen formation in retinal blood vessels, it leads to defective endothelial axial polarization and to the formation of severe vascular malformations in capillaries and veins. Tracking of Cdc42-depleted endothelial cells in mosaic retinas suggests that these capillary-venous malformations arise as a consequence of defective cell migration, when endothelial cells that proliferate at normal rates are unable to re-distribute within the vascular network.

KEY WORDS: Vascular malformations, Cdc42, Cell migration, Endothelial axial polarity, Angiogenesis, Proliferation

INTRODUCTION

The small GTPase cell division cycle 42 (Cdc42) is present in most eukaryotes, where it exerts basic functions in the regulation of actin-based morphogenesis and cell polarity (Boureux et al., 2007; Jaffe and Hall, 2005; Melendez et al., 2011). Cdc42 has also been implicated in a variety of other cellular processes in many different cell types (Etienne-Manneville, 2004; Hall, 1998; Heasman and Ridley, 2008; Melendez et al., 2011). The current comprehensive picture of Cdc42 function is inferred from an assemblage of data obtained from diverse cell types, species, experimental models and tools, which in most cases cannot be applied to any single cell type or stage of development. An example is angiogenesis – the process of new blood vessel formation from existing ones – and the role of Cdc42 in endothelial cells (ECs). Work with cultured ECs shows that Cdc42 regulates the actin cytoskeleton (Barry et al., 2015; Hall, 1998; Wójciak-Stothard et al., 1998), membrane protrusions (Kouklis et al., 2003), macro-pinocytosis (Tkachenko et al., 2004), adherence junctions and EC barriers (Broman et al., 2006), cell migration (Dormond et al., 2001; Sakabe et al., 2017; Vitorino and Meyer, 2008) polarization (Etienne-Manneville, 2004; Vitorino and Meyer, 2008) and tube formation (Bayless and Davis, 2002; Davis et al., 2011). It is unclear, however, if all of these cellular functions regulated by Cdc42 *in vitro* contribute to vascular morphogenesis *in vivo*.

Experiments in zebrafish and mice have provided some insights: in zebrafish, Cdc42 has been suggested to regulate filopodia formation and EC guidance mechanisms (Fantin et al., 2015; Kaur et al., 2006; Wakayama et al., 2015). In mice, constitutive [Tie2 (Tek – Mouse Genome Informatics)-Cre-mediated] EC-specific Cdc42 deletion leads to abnormal vascular morphogenesis, disrupted blood circulation and early embryonic death (Barry et al., 2015; Jin et al., 2013), making it difficult to discriminate between primary cellular consequences of Cdc42 deletion and secondary effects of a disrupted circulation. When Cdc42 deletion was instead induced at an early postnatal time point (Cdh5-Cre-mediated) and analyzed during retinal sprouting angiogenesis, it caused reduced EC filopodia formation (Barry et al., 2015; Sakabe et al., 2017), an effect also observed following pharmacological Cdc42 inhibition of Cdc42 (Fantin et al., 2015). Based on these observations, it has been suggested that Cdc42 plays a role in F-actin organization, with consequences for vascular apical basal polarity (Barry et al., 2015) and EC migration (Sakabe et al., 2017).

Here, using conditional and mosaic gene ablation, together with computational modeling, we aimed to further clarify which of the Cdc42-dependent cellular functions are relevant for vascular morphogenesis in the postnatal retina. Our work confirms some of the previously suggested EC roles of Cdc42 and adds a new role in axial polarization. We also show that loss of Cdc42 leads to vascular malformations specifically in capillaries and veins, locations in which EC proliferation is normally high. We suggest that these malformations arise as a consequence of the inability of Cdc42-depleted ECs to migrate away from these areas and disperse within the developing vascular network.

RESULTS

Cdc42 deletion causes capillary-venous malformations, with retained endothelial apical-basal polarity and enlarged vessel lumens

In order to avoid the secondary systemic consequences of embryonic vascular disruption, we induced EC-specific Cdc42 deletion in newborn mice and focused our analysis at the developing retina, an organ that allows simultaneous imaging of sprouting and remodeling of vessels with readily distinguishable arterio-venous

[1]Department of Immunology, Genetics and Pathology, Rudbeck Laboratory, Uppsala University, 75185 Uppsala, Sweden. [2]Laboratory of Angiogenesis and Vascular Metabolism, Department of Oncology, KU Leuven, Leuven, Belgium. [3]Laboratory of Angiogenesis and Vascular Metabolism, Vesalius Research Center, VIB, Leuven, Belgium. [4]Computational Biology Laboratory, Center for Vascular Biology Research, Beth Israel Deaconess Medical Center, Harvard Medical School, Boston, MA 02215, USA. [5]Biotech Research and Innovation Centre, University of Copenhagen, Ole Maaløes Vej 5, 2200 Copenhagen, Denmark. [6]Integrated Cardio Metabolic Centre (ICMC), Department of Medicine Huddinge, Karolinska Institute, Novum, SE-141 57 Huddinge, Stockholm, Sweden.

*Authors for correspondence (Konstantin.gaengel@igp.uu.se; Christer.Betsholtz@igp.uu.se)

C.B., 0000-0002-9342-1634; C.B., 0000-0002-8494-971X; K.G., 0000-0002-2682-2833

Received 3 November 2017; Accepted 24 May 2018

Development (2018) 145, dev161182. doi:10.1242/dev.161182

hierarchy. The mouse retina is vascularized by angiogenic sprouting (Fruttiger, 2002), which starts at postnatal day (P) 0 and is finished around P25 (Stahl et al., 2010). Early postnatal gene deletion therefore targets the developing retinal vasculature at a time when many other vascular beds are already well developed and generally less susceptible to the consequences of gene deletion. We established mice in which EC-specific deletion of *Cdc42* was tamoxifen-inducible [*Cdh5(PAC)-Cre^{ERT2};Cdc42$^{flox/flox}$*] (Pitulescu et al., 2010; Wu et al., 2006) (hereafter referred to as *Cdc42$^{i\Delta EC}$*) and also introduced *Rosa26-EYFP* (Srinivas et al., 2001) or *Rosa26-tdTomato(Ai14)* (Madisen et al., 2010) reporter alleles to allow visualization of Cre-mediated recombination at cellular resolution. Daily administration of tamoxifen for 3 days (P0-P2) caused a robust, albeit not complete, loss of endothelial *Cdc42* mRNA and protein at P7 and was chosen as the standard approach for our analysis (Fig. 1A-C). As shown below, the incomplete knockout (KO) of *Cdc42* mRNA and protein was a result of cellular mosaicism, i.e. a vasculature composed of a mixture of normal and Cdc42-depleted ECs [hereafter referred to as wild-type (WT)-EC and *Cdc42*-KO-EC, respectively] at variable proportions – an inherent but often neglected consequence of inducible gene deletion. Thus, *Cdc42$^{i\Delta EC}$* retinas might contain both WT-EC (Rosa26-YFP negative) and *Cdc42*-KO-EC (Rosa-26-YFP positive) (see Materials and Methods for a technical note on this approach).

At P7, *Cdc42$^{i\Delta EC}$* retinas displayed reduced vascular outgrowth and a significant shortening of arteries and veins (Fig. 1D,E). In addition, conspicuous vascular malformations were observed in veins and their neighboring capillary network. The malformed vessels were focally dilated and commonly formed vascular outpouchings (Fig. 1D,F). These malformations progressively expanded with time and assumed mulberry-like shapes at later developmental stages (Fig. 1G). Interestingly, we observed vascular malformations only in retinas where the proportion of Cdc42-depleted cells was ≥60% (i.e. ≥60% *Cdc42*-KO-EC and ≤40% WT-EC). This strongly suggests that the vascular malformations do not simply arise by local clonal expansion of mutant cells in a tumor formation-like process. Rather, a threshold proportion of Cdc42 mutant cells is required to initiate lesion formation, which subsequently also engages the WT cells. Notably, we never observed vascular malformations in arteries. Although they occasionally appeared constricted, they were not changed significantly in overall width (Fig. 1D,F).

We next analyzed whether the capillary-venous vascular malformations were blood-perfused hollow structures that retained apical-basal (A-B) polarity. Because several studies have reported a role for Cdc42 in A-B polarization of epithelia (Martín-Belmonte et al., 2008; Wan et al., 2013; Elias et al., 2015; Kesavan et al., 2009) and ECs (Barry et al., 2015), and because A-B polarity is considered a prerequisite for lumen formation in epithelial tissues and blood vessels (Martín-Belmonte et al., 2007; Davis et al., 2011), we expected to find A-B polarity defects in *Cdc42$^{i\Delta EC}$* retinal vessels. Surprisingly, however, we failed to find convincing defects in A-B polarization and vascular lumen formation. The apical markers ICAM2 (Bradley et al., 1995) and podocalyxin/GP135 (Podxl) (Horvat et al., 1986; Meder et al., 2005) were both consistently localized at the luminal side of ECs, whereas the basement membrane protein collagen IV (Laurie et al., 1983) delineated the abluminal surface also at vessel stretches composed mostly of *Cdc42*-KO-EC, including the capillary-venous malformations (Fig. 1I, Fig. S1A, Movies 1-8). Blood vessels in *Cdc42$^{i\Delta EC}$* retinas were generally lumenized, with the exception of remodeling or regressing capillaries. The hollow cavernous outpouchings of the capillary-venous malformations were connected by continuous lumens and were delineated by a single layer of ECs that exhibited seemingly normal A-B polarization (Fig. 1H,I, Movies 1-11). These results suggest that during postnatal angiogenesis of the retina, Cdc42 might not strictly be required for A-B polarization of ECs, nor for vascular lumen formation. Our data instead suggest an important role of Cdc42 in restricting vessel diameter and in prohibiting the formation of capillary-venous malformations. We further investigated whether the loss of Cdc42 directly affected endothelial cell survival, as suggested by studies of Cdc42 KO embryos (Jin et al., 2013). Using the early apoptosis marker cleaved caspase 3, we found no evidence for increased EC apoptosis in *Cdc42$^{i\Delta EC}$* retinas (Fig. S1B,C). Our data are in agreement with observations suggesting that EC apoptosis in the embryo occurs secondary to disrupted circulation in Cdc42 KO embryos (Barry et al., 2015).

Cdc42 is required for endothelial tip cell selection and filopodia formation

Because the delayed radial expansion of the *Cdc42$^{i\Delta EC}$* retinal vasculature (Fig. 1D,E) suggests problems with angiogenic sprouting, we studied this process in more detail. We took advantage of the individually variable degrees of *Cdc42* deletion in *Cdc42$^{i\Delta EC}$* retinas to analyze the behavior of *Cdc42*-KO-EC in mosaic vessels with different proportions of WT-EC. We first characterized the mosaicism with regard to Cre-activated *Rosa26-EYFP* and found that recombination was highly variable (11-95%) between individual retinas. YFP$^+$ WT-EC distributed randomly throughout the retinal vasculature (Fig. 2A,B), as shown by the equal proportions of recombined cells at tip (TR) and stalk (SR) positions (TR/SR≈1) (Fig. 2C-E). In contrast, *Cdc42*-KO-EC were significantly underrepresented at tip positions (TR/SR≈0.3) (Fig. 2A,B,D,E). In retinas with low proportions of *Cdc42*-KO-EC, no mutant cells occurred within several hundred micrometers from the vascular sprouting front (Fig. 2A,B). This distance decreased with increasing recombination rate, but even in highly recombined retinas where mutant cells were forced to assume tip cell positions, their disadvantage at this location was evident (Fig. 2B, bottom row). A reduced TR/SR ratio was also observed in *Cdc42$^{i\Delta EC}$* aortic ring explant cultures (Fig. S2A,B) and was obvious even at the high recombination rate (90±0.04%) that we achieved in those experiments (see Materials and Methods for details). These results demonstrate that *Cdc42*-KO-EC have a competitive disadvantage to assume tip positions in angiogenic sprouts, suggesting a crucial and cell-autonomous requirement for Cdc42 in tip cell selection.

Endothelial tip cells protrude actin-rich filopodia (Gerhardt et al., 2003) (Figs 2C and 3A), which have been proposed to sense the environment and direct vascular growth towards sources of VEGF proteins, anchor tip cells to extracellular substrates, pull the angiogenic sprout forward and facilitate the formation of anastomoses with other ECs (De Smet et al., 2009; Gerhardt et al., 2003). *Cdc42*-KO-EC at tip positions lacked filopodia and instead protruded a few short studded processes from their surfaces (Fig. 3A-D). Neighboring WT-EC tip cells, on the other hand, displayed normal filopodial extensions, demonstrating that Cdc42 is cell-autonomously required for filopodia formation (Fig. 3A). The morphologies of *Cdc42*-KO-EC at tip cell positions ranged between two extremes (Fig. 3E), a rounded lumenized cell (Fig. 3E, middle row, Movies 9 and 10) or a nonlumenized cell with abnormally elongated shafts (Fig. 3E, bottom row). Irrespective of their

Development (2018) 145, dev161182. doi:10.1242/dev.161182

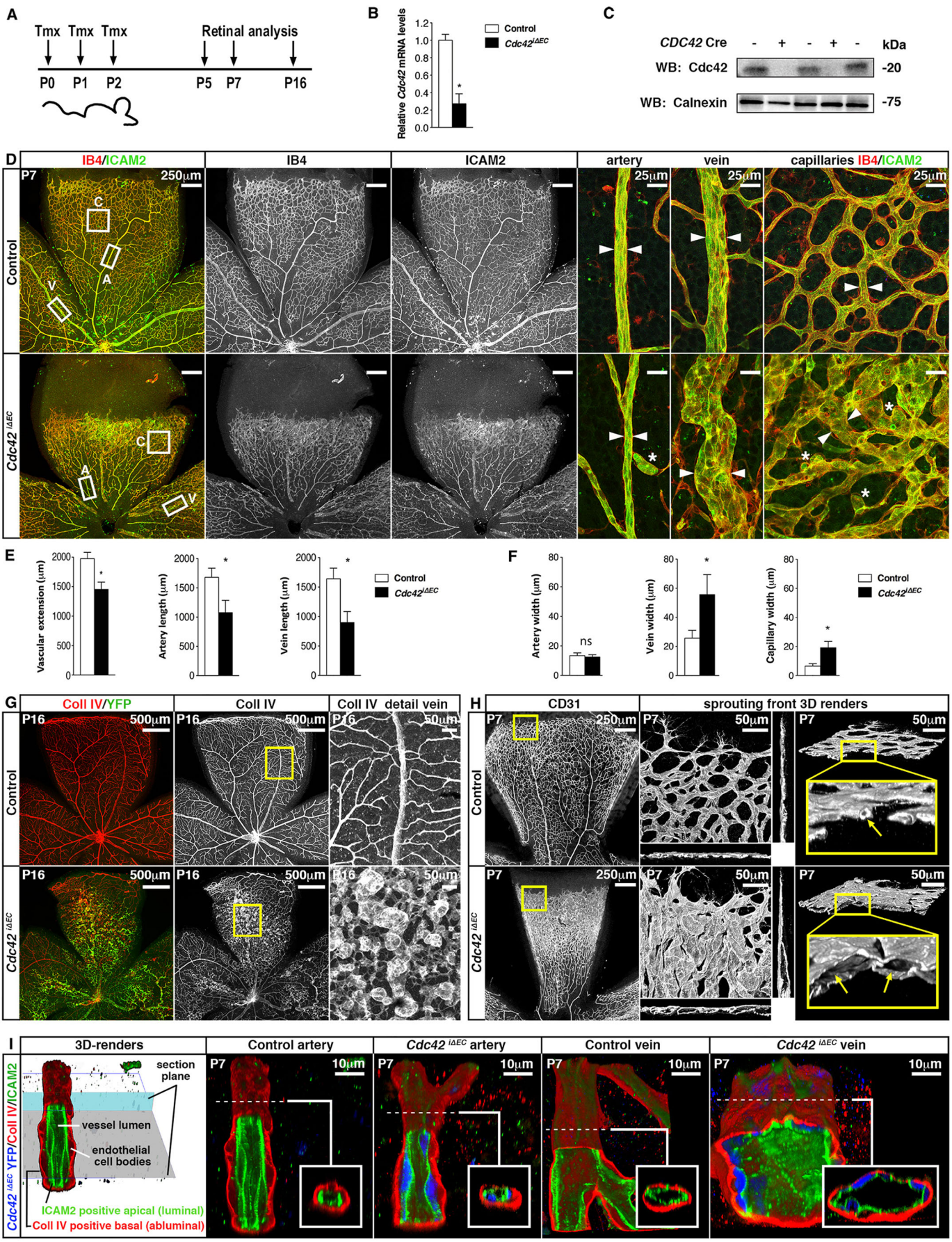

Fig. 1. See next page for legend.

Development (2018) 145, dev161182. doi:10.1242/dev.161182

Fig. 1. Endothelial-specific *Cdc42* deletion causes capillary-venous malformations with retained endothelial A-B polarity and enlarged vessel lumens. (A) Experimental outline: endothelial specific *Cdc42* deletion was induced via tamoxifen (Tmx) administration (P0-P2) and retinas were analyzed at P5, P7 and P16. (B) Quantitative reverse transcription polymerase chain reaction (qRT-PCR) analysis of *Cdc42* mRNA, performed on freshly isolated brain ECs at P7 from control (n=10) and $Cdc42^{i\Delta EC}$ (n=6) mice. (C) Western blot analysis of Cdc42 protein levels from control (n=3) and $Cdc42^{i\Delta EC}$ (n=2) mice. (D) P7 retinal whole mounts. Blood vessels and vascular lumens are visualized by IB4 and ICAM2 staining, respectively. Leftmost column: note the reduced vascular expansion towards the retinal periphery and vascular malformations in veins (V) and capillaries (C), but not in arteries (A) of $Cdc42^{i\Delta EC}$ retinas. Rightmost columns: high-resolution images of boxed areas reveal tortuous dilations in vein and capillaries (arrowheads), and protuberant endothelial structures (asterisks). (E) Quantification of vascular extension (n=9) and arterial and venous length (n=3). (F) Quantification of arterial, venous and capillary width (n=3). (G) P16 control and $Cdc42^{i\Delta EC}$ retinas stained with collagen IV (Coll IV) and YFP (a reporter for Cre-mediated recombination). Boxed areas in middle column highlight veins and adjacent capillaries and are shown in high resolution to the right. Note the mulberry-like malformations in $Cdc42^{i\Delta EC}$ retinas. (H) High-resolution 3D reconstruction of confocal images from P7 control and $Cdc42^{i\Delta EC}$ retinas stained with CD31. Boxed areas in overview images (left column) are shown in high resolution in the middle column. Optical Z-sections below and to the right show enlarged vascular lumens in a $Cdc42^{i\Delta EC}$ retina (middle column). Tilted views of 3D reconstructions of the middle column are shown to the right: boxed areas are shown in high resolution and reveal vascular lumens (yellow arrows). Note abnormally dilated capillary vessels and cavernous malformations in the $Cdc42^{i\Delta EC}$ retina (see also Movies 9-11). (I) 3D reconstructions and single optical Z-sections of arteries and veins from P7 control and $Cdc42^{i\Delta EC}$ retinas. Dashed lines indicate the location of the cross-sectional view shown in the boxed areas. Vessels are displayed partially sectioned as indicated in the leftmost panel. ICAM2 (green) marks the apical (luminal) surface of blood vessels, while Coll IV stains the basal (abluminal) surface. Note that A-B polarization of blood vessels in $Cdc42^{i\Delta EC}$ retinas appears normal and that YFP^+ (*Cdc42*-KO-EC) cells (blue) are properly located between the apical and basal domains (see also Movies 1-8). Graphs show mean±s.d. (unpaired two-tailed Student's *t*-test; ns, nonsignificant; $^*P \leq 0.05$.

morphology, *Cdc42*-KO-EC at the tip cell position consistently lacked filopodia.

We next tested whether *Cdc42*-KO-EC could be forced to adopt tip cell characteristics and extend filopodia through inhibition of Notch signaling. The pharmacological gamma secretase inhibitor N-[N-(3,5-difluorophenacetyl)-L-alanyl]-S-phenylglycerin t-butyl ester (DAPT) normally increases tip cell and filopodia numbers in the developing retina (Hellström et al., 2007), but failed to do so in $Cdc42^{i\Delta EC}$ retinas (Fig. S3A,B). Interestingly, however, DAPT treatment greatly enhanced the severity of the capillary-venous malformations in $Cdc42^{i\Delta EC}$ retinas (Fig. S3C). This aspect is further discussed below.

Because *in vitro* studies have reported rapid and dramatic cellular changes upon Cdc42 disruption (Kroschewski et al., 1999; Nobes and Hall, 1995), the question arose as to what extent the phenotypes observed in $Cdc42^{i\Delta EC}$ retinas at P7 could reflect vascular adaptations. We therefore studied the vascular phenotypes in $Cdc42^{i\Delta EC}$ retinas 2 days earlier and found that all key abnormalities observed at P7 were already present at P5, including reduced vascular extension, formation of capillary-venous malformation, inability of *Cdc42*-KO-EC to form filopodia and assume tip cell positions (Fig. S4A-F). Similar to the situation at P7, we did not find evidence for an increase in EC apoptosis in $Cdc42^{i\Delta EC}$ retinas at P5 (Fig. S4G,H).

Effects on cellular junctions

Differential vascular endothelial cadherin [VE-cadherin (Cdh5)] dynamics at EC junctions has been proposed to drive cell re-arrangements during angiogenic sprouting (Bentley et al., 2014a). A role for Cdc42 in EC junction formation has been proposed *in vitro* (Broman et al., 2006) and during embryonic development (Barry et al., 2015). In agreement with these observations, we found that VE-cadherin localization was altered in $Cdc42^{i\Delta EC}$ retinal vessels, irrespective of vessel type, but to a variable extent (Fig. 4A). Importantly, these defects were not strictly cell-autonomous, because WT-EC in chimeric vessels also showed abnormal junctional VE-cadherin staining (see Fig. 4A for examples). In contrast, junctional localization of another EC adhesion molecule, cluster of differentiation 31 (CD31/PECAM1), was unaffected in $Cdc42^{i\Delta EC}$ retinas (Fig. 4B). Immunolabeling of the junction-associated proteins zonula occludens-1 (ZO-1) and β-catenin was technically problematic in whole-mounted retinas, and we therefore analyzed these proteins only in confluent primary cultures of *Cdc42*-KO-EC. In these conditions, VE-cadherin, β-catenin and ZO-1 were all localized to cellular junctions in *Cdc42*-KO-EC, but, in contrast to WT-EC, their junctions appeared thinner, while remaining continuous (Fig. 4C). The wide junction labeling observed in WT-EC under these culture conditions might reflect ongoing junctional remodeling (Abu Taha and Schnittler, 2014). Thus, *Cdc42*-KO-EC junctions appear less active or less able to remodel, albeit not necessarily unstable. We also analyzed mosaic cultures of *Cdc42*-KO-EC and WT-EC and found that individual WT-EC formed morphologically different contacts with neighboring WT-EC or *Cdc42*-KO-EC, respectively. Whereas the contacts between WT-ECs were normally wide, the contacts between WT-EC and adjacent *Cdc42*-KO-EC were thin and indistinguishable from the junctions formed between two adjacent *Cdc42*-KO-EC (Fig. 4D). This suggests that junctional defects in *Cdc42*-KO-EC may have dominant non-cell-autonomous effects on the behavior of neighboring WT-EC. The observed defects in VE-cadherin localization are, however, unlikely to have a significant impact on the formation of vascular malformations, because arteries did not dilate or develop malformed vascular structures, in spite of abnormal VE-cadherin localization (Fig. S5).

Cdc42 controls endothelial axial polarity in a vessel-type specific manner

Because we failed to find clear evidence for A-B polarization defects in $Cdc42^{i\Delta EC}$ retinas, we asked whether other types of polarization could be affected. ECs have also been reported to polarize perpendicular to their A-B axis, referred to as axial (Franco et al., 2015), front-rear (Dubrac et al., 2016) or planar cell polarity (PCP) (Devenport, 2014; Lee and Bautch, 2011). We first assessed EC axial polarization in conjunction with EC migration in scratch wound assays *in vitro*. The hallmark of this process is re-orientation of the microtubule organizing centers (MTOCs) and Golgi complex in the direction of cell migration (Kupfer et al., 1982) (Fig. 5A,B), which is considered a prerequisite for subsequent collective cell migration (Vitorino and Meyer, 2008). In the scratch wound assay, axial polarization first occurs in pioneer cells that emerge at the scratch border. Neighboring cells subsequently re-orient and follow the pioneers through drag forces (Kupfer et al., 1982). A crucial role for Cdc42 in this type of polarity was earlier suggested by Vitorino and colleagues using small interfering RNA-mediated knockdown of Cdc42 in human umbilical vein endothelial cells (Vitorino and Meyer, 2008). In order to stay as close as possible to the *in vivo* situation, we assessed axial polarity in scratch wound assays performed on primary brain ECs isolated from $Cdc42^{i\Delta EC}$ mice. We determined EC polarization towards the wound, considering the nucleus-Golgi axis angle (Fig. 5A,B). Five hours after scratching, we found that the majority of WT cells in the first to third rows

Development (2018) 145, dev161182. doi:10.1242/dev.161182

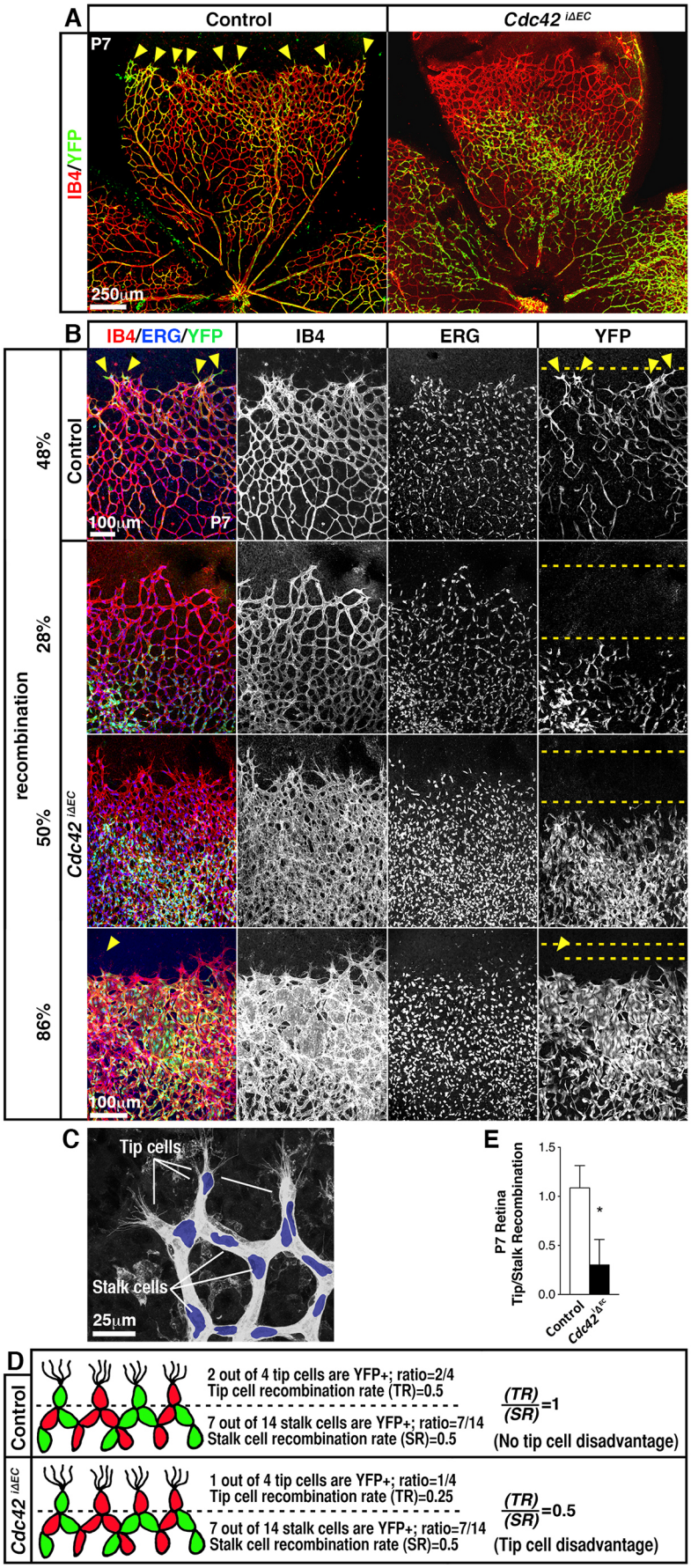

Fig. 2. Cdc42 is required for endothelial tip cell selection. (A) Distribution of recombinant cells (YFP$^+$) in P7 control and *Cdc42*$^{i\Delta EC}$ retinas stained for EC (IB4) and YFP. Yellow arrowheads indicate recombined endothelial tip cells (YFP$^+$). (B) Images of sprouting front areas in P7 control and *Cdc42*$^{i\Delta EC}$ retinas with different degrees of recombination stained for EC (IB4), recombinant cells (YFP$^+$) and EC nuclei (ERG). Yellow arrowheads indicate recombinant endothelial tip cells (YFP$^+$) and dashed lines mark vascular areas devoid of recombinant cells. (C) Example of tip and stalk cells in a P7 control retina. Filopodia and EC outlines are visualized by IB4 staining; the positions of EC nuclei are indicated in blue. (D) Schematic representation of the calculations used to determine tip cell disadvantage. The overall recombination rate in retinas, referred to as stalk cell recombination (SR), was calculated as the percentage of YFP$^+$ vascular area (YFP$^+$/IB4 area×100). The tip cell recombination (TR) was calculated as the percentage of recombined tip cells (number YFP$^+$/total number of tip cells×100) (E) Quantification of TR/SR ratios in control (n=7) and *Cdc42*$^{i\Delta EC}$ (n=9) retinas. Graphs show mean±s.d. (unpaired two-tailed Student's t-test, *$P\leq0.001$.

Development (2018) 145, dev161182. doi:10.1242/dev.161182

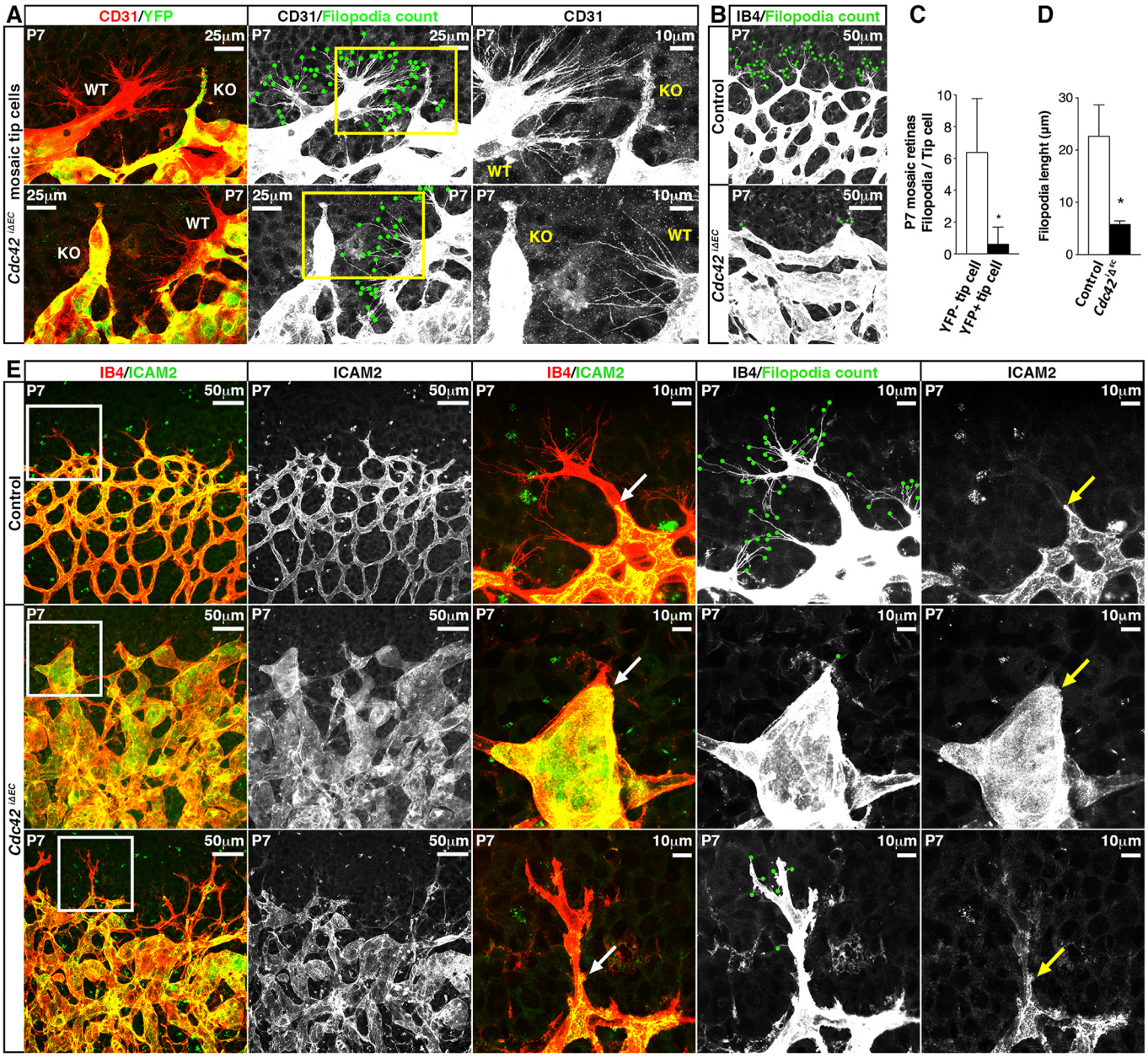

Fig. 3. Cdc42 is required for filopodia formation and normal tip cell shape. (A) Analysis of tip cells in highly recombinant (>80%) *Cdc42*$^{i\Delta EC}$ mosaic retinas at P7. ECs and their filopodia are visualized by CD31 and recombined cells are marked by YFP. Middle column: green dots denote filopodia. Yellow boxes indicate the wild-type (WT) and *Cdc42* KO (KO) tip cells, shown at high resolution in the right column. (B) Sprouting front areas of control and high degree recombined *Cdc42*$^{i\Delta EC}$ retinas. ECs and filopodia are visualized by IB4; filopodia are indicated by green dots. (C) Quantification of filopodia number per tip cell of YFP^{-} (WT) and YFP^{+} (*Cdc42* KO) ECs in highly recombined *Cdc42*$^{i\Delta EC}$ retinas (n=10, with more than 380 tip cells analyzed; *P<0.001). (D) Quantification of filopodia length (μm) per tip cell in WT and *Cdc42* KO tip cells in *Cdc42*$^{i\Delta EC}$ retinas (n=3, *P<0.01). (E) Sprouting front of control [*Cdh5(PAC)-Cre*^{ERT2}; *Rosa26-EYFP*] and highly recombined (>80%) *Cdc42*$^{i\Delta EC}$ P7 retinas stained with IB4 and ICAM2. Boxed areas are magnified in right columns. Note that whereas control tip cells are ICAM2^{-} and extend filopodia (indicated by green dots), *Cdc42*-KO-EC at tip cell positions are morphologically abnormal, ranging between two phenotypic extremes: a rounded cell shape with extended ICAM2^{+} lumens or a thin, elongated, ICAM2^{-}, nonlumenized shape. Arrows indicate the extension of ICAM2^{+} vascular lumens. In both phenotypic variations, ECs lacking Cdc42 (*Cdc42*-KO-EC) present very few filopodia. Graphs show mean±s.d. (unpaired two-tailed Student's *t*-test).

polarized within ±45° perpendicular to the wound border, with a slight lag in the third row. In contrast, the majority of *Cdc42*-KO-EC failed to polarize towards the wound (Fig. 5B,C,D, Table S1A). At 24 h postscratching, polarization of WT cells had further improved in the third row, whereas polarization of *Cdc42*-KO-EC did not improve with time in any row (Fig. 5B,C,D, Table S1A).

EC axial polarization is also observed *in vivo* (schematic representation in Fig. 6A,B) and has been reported to correlate with the direction of blood flow (Franco et al., 2015). To investigate whether the loss of Cdc42 influences EC axial polarity *in vivo*, we analyzed the Golgi orientation in arteries, veins and capillaries of WT and *Cdc42*$^{i\Delta EC}$ retinas (Movie 12 shows how polarity was determined). This analysis confirmed EC polarization against the predicted blood flow direction in WT retinas and showed that EC axial polarity was specifically disturbed in veins and capillaries, but not in arteries of *Cdc42*$^{i\Delta EC}$ retinas (Fig. 6C-G, Table S1B). We

Development (2018) 145, dev161182. doi:10.1242/dev.161182

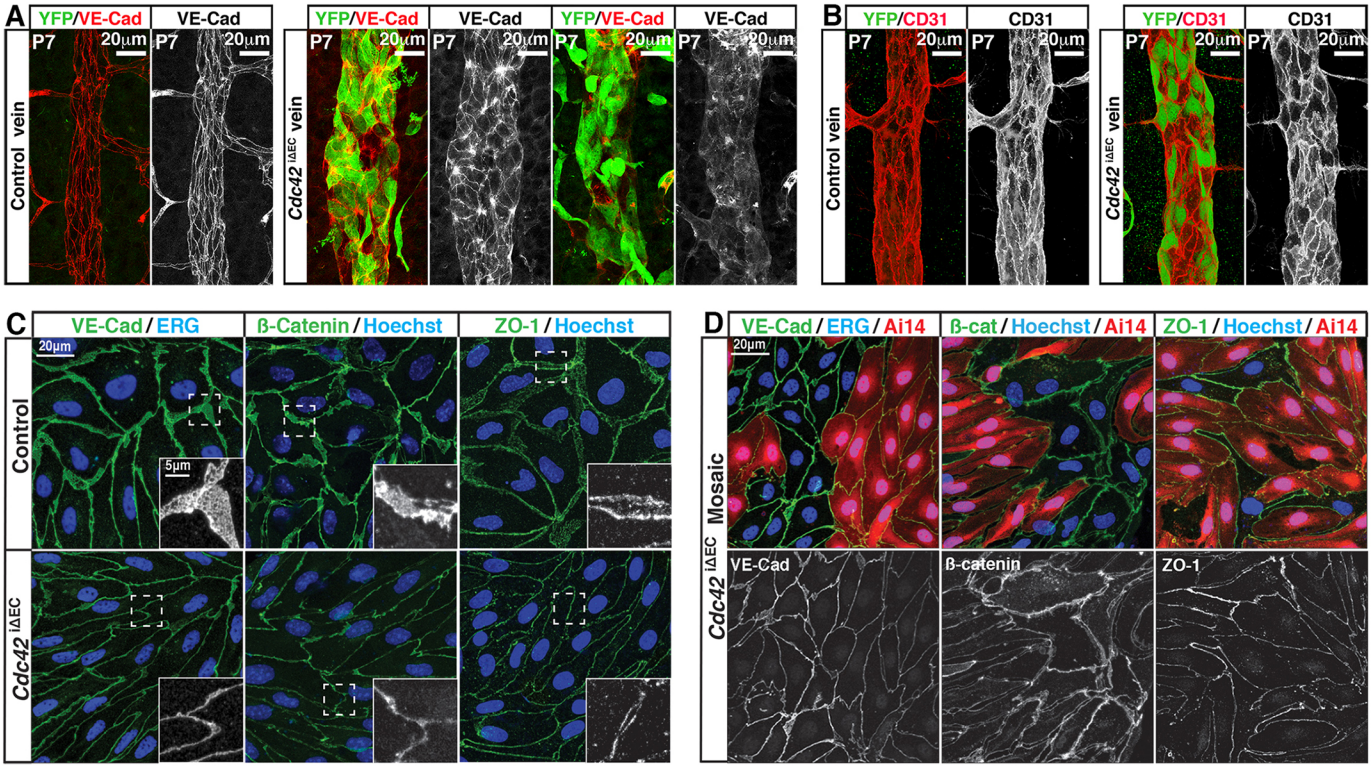

Fig. 4. Effects on EC junctions in the absence of Cdc42. (A,B) Confocal images of P7 control and *Cdc42*$^{i\Delta EC}$ veins stained for YFP, VE-cadherin (red in A) and CD31 (red in B). *Cdc42* deficiency leads to disturbed VE-cadherin localization at EC junctions *in vivo* (A). Effects can range from a partial (middle panels) to severe loss of VE-cadherin (right panels). Junctional localization of CD31 is not affected in the absence of *Cdc42* (B). (C) Confocal images of cultured primary brain ECs, isolated from P7 control and *Cdc42*$^{i\Delta EC}$ mice, stained with Hoechst or ERG and VE-cadherin, β-catenin and ZO-1. Note that junctional staining of VE-cadherin, β-catenin and ZO-1 appear thinner but continuous in ECs lacking *Cdc42* (*Cdc42*-KO-EC). (D) Mosaic cultures of P7 control and *Cdc42* KO primary brain ECs stained with Hoechst or ERG and VE-cadherin, β-catenin and ZO-1. Recombination (and thus loss of *Cdc42*) is indicated by the Ai14 reporter (red). Note that cellular junctions between control and *Cdc42*-KO-EC appear thinner and dimmer than junctions between control ECs.

used the central-peripheral axis as a proxy for flow direction in arteries and veins (Fig. 6A). In the capillary plexus at the sprouting front, flow has been predicted to be dynamically changing direction (Franco et al., 2015). When analyzing the three most distal EC rows (i.e. tip cells and the two proximal stalk cells rows), we observed a dual-oriented polarity pattern in WT retinas, in which approximately half of the ECs oriented towards the retinal periphery and the other half towards the center. This pattern was lost in *Cdc42*$^{i\Delta EC}$ retinas, where EC polarization instead appeared random (Fig. 6C,F,G, Table S1B).

To obtain further molecular insight into how Cdc42 regulated EC axial polarity, we analyzed the subcellular localization of members of the Par3/Par6 (Pard6a)/aPKC complex. In epithelial cells, Par complex proteins become enriched in areas in which polarity is subsequently established (Etienne-Manneville, 2004); inhibition of Cdc42 has been shown to prevent this enrichment in *Caenorhabditis elegans* (De Smet et al., 2009). When analyzing the subcellular localization of Par3 and aPKCζ in WT-EC in the context of the scratch wound assays, we observed that both Par3 and aPKCζ were localized to cellular junctions and membrane protrusions. In contrast, this localization was lost in *Cdc42*-KO-EC (Fig. S6), suggesting that Cdc42 controls EC axial polarity, at least in part, through localization of the Par complex.

Cdc42 is required for EC motility and directed migration and regulates the actin cytoskeleton

Sprout extension, shuffling of tip cells, branch anastomosis and regression collectively shape the growing vascular network during angiogenesis. These processes require cytoskeletal rearrangement and EC migration (Franco et al., 2015; Geudens and Gerhardt, 2011), functions known to be regulated by Cdc42 in various cell types (Hall, 1998) including ECs (Sakabe et al., 2017; Vitorino and Meyer, 2008). Indeed, the delayed vascular outgrowth observed in *Cdc42*$^{i\Delta EC}$ retinas (Fig. 1D,E) suggested impaired endothelial motility. Because real-time analysis of angiogenic sprouting in the postnatal mouse retina is technically challenging, we used three different *in vitro* assays to analyze EC motility and directed migration. To allow unambiguous identification of ECs in those assays, we bred Cldn5-GFP mice [which express green fluorescent protein (GFP) specifically in ECs] to *Cdc42*$^{i\Delta EC}$ and control mice and subsequently isolated aortas and primary brain ECs. We further used the *Rosa26-tdTomato(Ai14)* reporter (Madisen et al., 2010) as a marker for recombination efficiency. Based on the *Rosa26-tdTomato(Ai14)* reporter, we obtained a high degree of recombination in both aortic rings (90±0.04%) and isolated ECs (80.8±12.02%). Time-lapse movies of aortic ring cultures showed that sprouting from *Cdc42*$^{i\Delta EC}$ explants was significantly altered, including reduced sprout number and length, as well as an increased numbers of branch points (Fig. 7A,C, Movies 13 and 14). Cell tracking showed that overall sprout elongation was slower in *Cdc42*$^{i\Delta EC}$ explants and that sprouts displayed slow movements with reduced directionality compared to controls (Fig. 7A,C, Movies 13 and 14). In order to understand whether Cdc42 was specifically required for the coordinated cell movements in angiogenic sprouts, or generally needed for EC motility, we tracked individual cell movements in 2D cultures of primary brain ECs isolated from

Development (2018) 145, dev161182. doi:10.1242/dev.161182

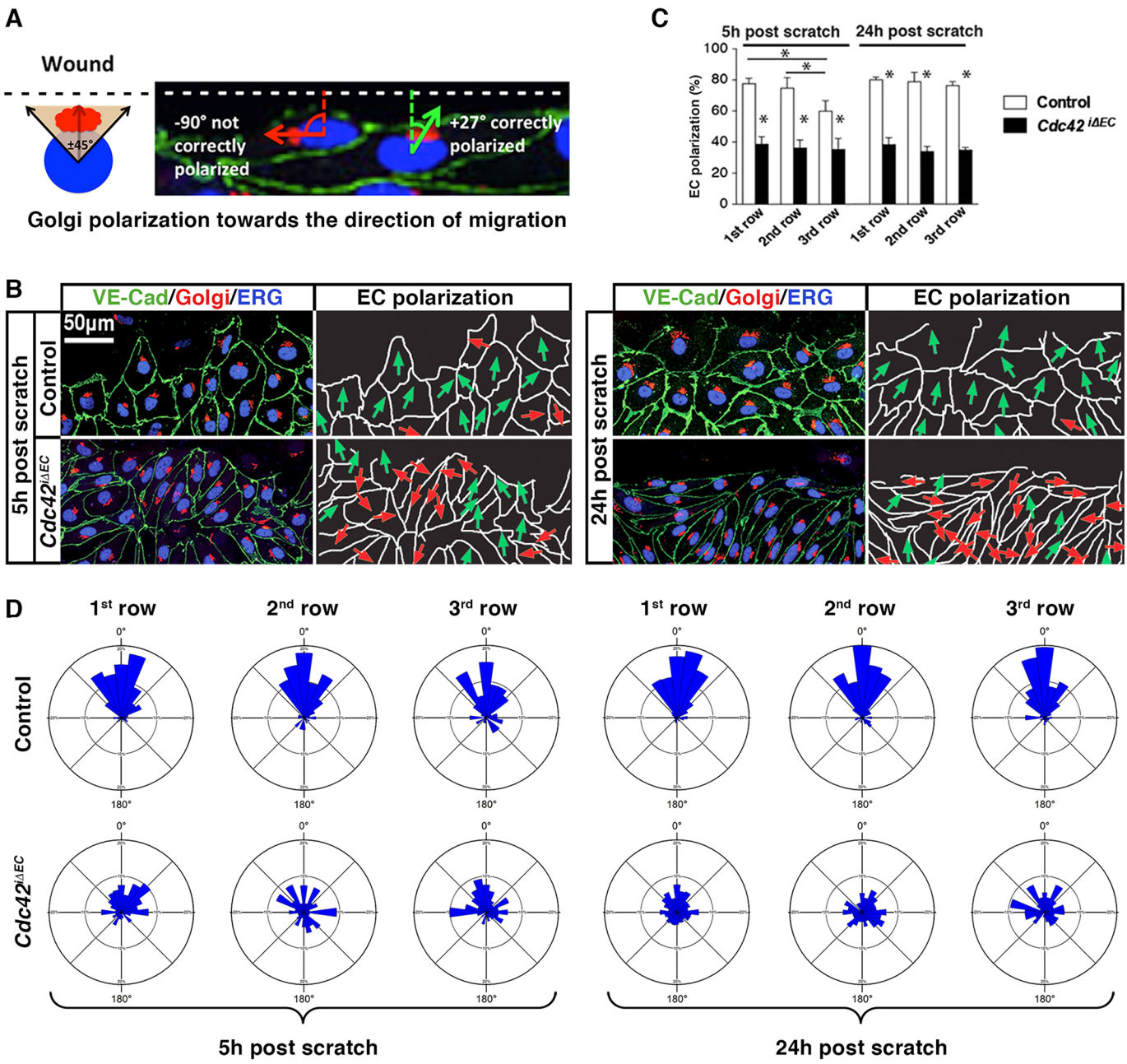

Fig. 5. Cdc42 is required for endothelial cell polarization during directed cell migration. (A) Illustration of Golgi polarization towards the direction of migration in a scratch wound assay (nuclei in blue, Golgi in red, junctions in green). EC polarization was determined with the wound as reference and considering the nucleus-Golgi axis angle as correctly polarized (<±45° towards the wound) or not correctly polarized (>±45° towards the wound). (B) Confocal images of primary brain ECs of P7 control and *Cdc42*$^{i\Delta EC}$ mice at 5 h or 24 h postscratch, stained for ERG, GM130 (Golgi) and VE-cadherin (VE-Cad). Right panels illustrate EC axial polarization based on position of Golgi versus nucleus in the direction of migration; green arrows indicate correctly polarized ECs and red arrows indicate incorrectly polarized ECs. (C) Quantification of EC polarization towards the wound (% of cells/scratch wound analyzed) at 5 h (control n=8; *Cdc42*$^{i\Delta EC}$ n=11) and 24 h (control n=10; *Cdc42*$^{i\Delta EC}$ n=8) after the scratch in the first, second and third cell rows; >180 cells were analyzed per group (see Table S1A for quantification details); *P<0.001). (D) Rose diagrams showing polarization angles of ECs at 5 h and 24 h after scratch. Graphs show mean±s.d. (unpaired two-tailed Student's t-test).

Cdc42$^{i\Delta EC}$ mice or controls. Whereas WT-EC in subconfluent cultures displayed a scattering behavior, *Cdc42*-KO-EC stayed attached in groups that displayed slow, wiggly and seemingly randomized movements (Fig. 7B,D, Movies 15 and 16), indicating a general requirement of Cdc42 for EC motility. EC migration speed was also analyzed in scratch wound assays, which revealed an impaired ability of *Cdc42*-KO-EC to migrate (Fig. 7E,F, Movies 17 and 18). Together, these analyses show that general cell motility, directed cell migration and the ability to uphold migratory directionality are all significantly compromised in *Cdc42*-KO-EC.

Cdc42 is a key regulator of the actin cytoskeleton (Hall, 1998), and it is generally assumed that this function accounts for its role in cell motility and migration (Jaffe and Hall, 2005). As expected, we found several signs of cytoskeletal abnormality in *Cdc42*-KO-EC. Stress fibers were scarce and discontinuous (Fig. 7G, green arrowhead) and actin accumulations at the leading edge of

Development (2018) 145, dev161182. doi:10.1242/dev.161182

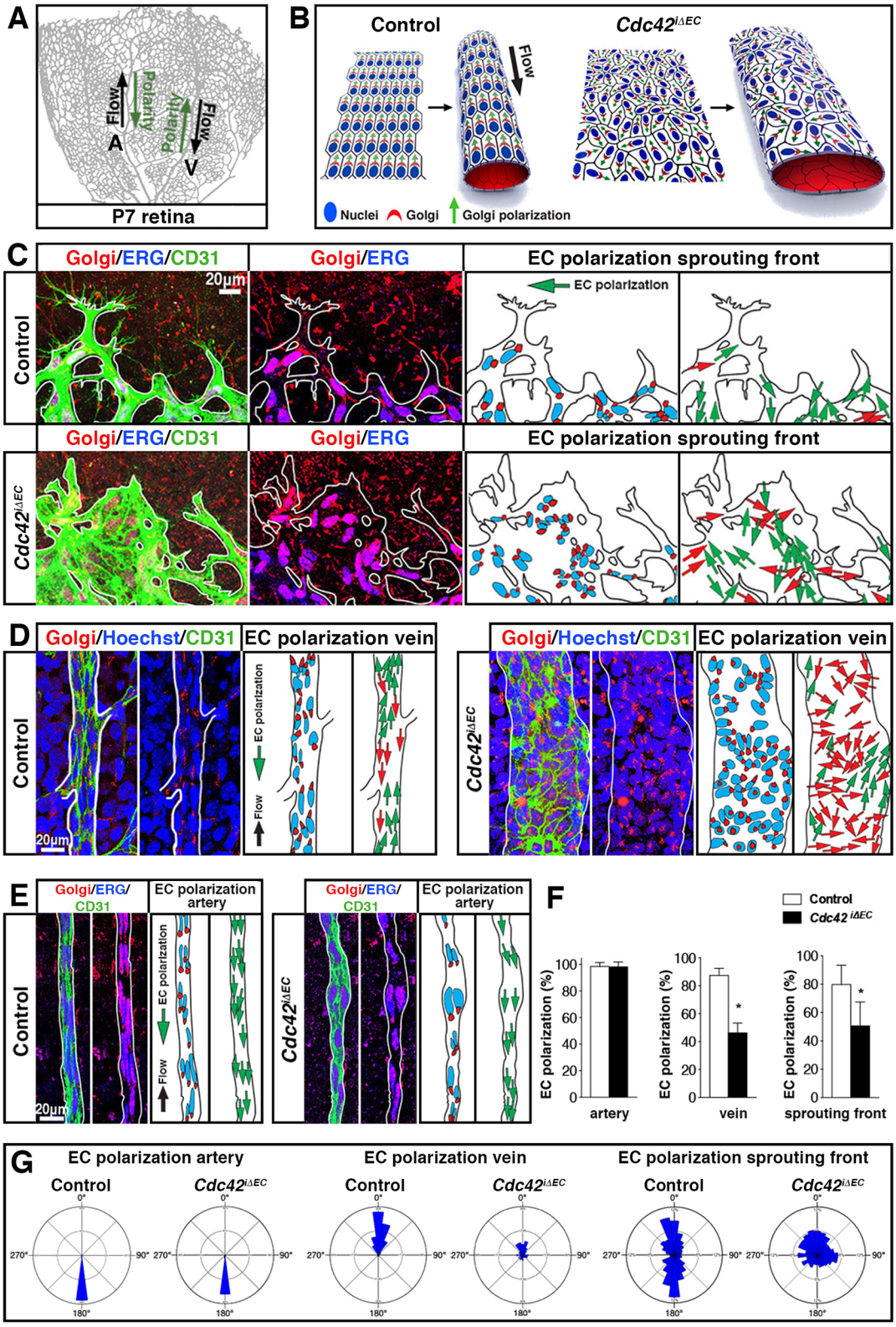

Fig. 6. See next page for legend.

migrating cells, as well as actin structures in the few remaining cellular protrusions, were substantially decreased (Fig. 7G, yellow arrowhead). Interestingly, junctional actin cables were less affected; they appeared thinner but were continuous (Fig. 7G, red arrowhead). In addition, paxillin, an intracellular adaptor protein propagating signals from integrins and growth factor receptors in the regulation of cell motility (López-Colomé et al., 2017), was diffusely distributed in the cytoplasm of *Cdc42*-KO-EC, as opposed to its concentration at focal adhesions and along filamentous actin structures in WT-EC (Fig. 7H).

Development (2018) 145, dev161182. doi:10.1242/dev.161182

Fig. 6. Endothelial axial polarity is disturbed in veins and capillaries of *Cdc42*$^{i\Delta EC}$ retinas. (A) Schematic representation of presumed blood flow (black arrows) and corresponding EC polarization (green arrows) in retinal arteries (A) and veins (V). (B) Schematic representation of EC axial polarization in 2D and how it translates into a 3D vessel. (C-E) Confocal images of capillaries in the sprouting front (C), veins (D) and arteries (E) of P7 control and *Cdc42*$^{i\Delta EC}$ retinas stained for ECs (CD31), EC nuclei (ERG/Hoechst) and Golgi (Golph4). Right panels are schematic illustrations of EC polarization: nuclei (blue), Golgi (red) and polarization direction (green arrows indicate correctly polarized ECs; red arrows indicate incorrectly polarized ECs) (see Movie 12 for how EC axial polarity was determined). (F) Quantification of EC polarization in arteries and veins [control (n=3); *Cdc42*$^{i\Delta EC}$ (n=3); *P<0.05] and capillaries of the sprouting front [control (n=6); *Cdc42*$^{i\Delta EC}$ (n=6)] from P7 control and *Cdc42*$^{i\Delta EC}$ retinas. In arteries and veins, ECs were considered correctly polarized when the Golgi oriented within ±45° against the predicted flow direction. In capillaries of the sprouting front, ECs were considered correctly polarized when oriented within ±45° towards the retinal center or the periphery. The percentage of correctly polarized ECs was determined in arteries and veins (green arrows in right panels in D and E), and for the three most distal EC rows in the sprouting front (i.e. tip cells and the two proximal stalk cell rows; green arrows in right panel in C); *P<0.05 (see Table S1B for quantification details). (G) Rose diagrams showing polarization angles of ECs from P7 control and *Cdc42*$^{i\Delta EC}$ arteries, veins and capillaries at the sprouting front. Graphs show mean±s.d. (unpaired two-tailed Student's t-test, * P≤0.05).

Integrated *in silico* modeling predicts that disrupted filopodia and axial polarity primarily drive the Cdc42 sprouting phenotype

To investigate the degree to which individual Cdc42-regulated cellular processes contribute to angiogenic sprouting alone or in combination, we exploited predictive computational modelling (Fig. 8A). We utilized the memAgent-Spring model (MSM) in original and extended forms, previously shown to be highly predictive *in vivo* (Bentley et al., 2014b; Bentley and Chakravartula, 2017) (see Materials and Methods for details).

Calibrating the model to the reduction in filopodia ($Cdc42_{FIL}$) observed *in vivo* (Fig. S7A,B) was sufficient to reproduce the tip cell disadvantage and horizontal (rear-front) segregation of *Cdc42*-KO-EC *in silico*, with striking agreement (Fig. 8B,D, Movie 20). Surprisingly, the simulations also predicted unequal vertical (top-bottom) segregation of WT and *Cdc42*-KO-EC in the vessel, as the mutant cells also lose the competition for the VEGF protein source provided by the astrocyte network, which is much stronger below the vessel (Fig. 8G,H, Movie 20). We subsequently confirmed vertical cell segregation *in vivo* (Fig. 8K,L, Movie 21), a phenotype that would otherwise have escaped notice.

Both horizontal and vertical segregation occurred when the EC axial polarity-sensing ability was reduced on its own ($Cdc42_{POL}$) by 75% (Fig. 8E,I, Fig. S7C, Movie 22). When filopodia and EC axial polarity were disrupted simultaneously ($Cdc42_{FIL/POL}$) (Fig. 8F,J, Movie 23) a stronger segregation was observed than with $Cdc42_{FIL}$ and $Cdc42_{POL}$ alone, requiring only a 30% reduction in polarity (Fig. S7D) and suggesting that the processes might synergize.

As our experiments revealed a moderate reduction of junctional actin (Fig. 7G,H) and abnormal EC junctions in *Cdc42*-KO-EC (Fig. 4), we also modeled the effects of changes in the junctional actin cortex ($Cdc42_{COR}$) and cell adhesion ($Cdc42_{ADH}$). We found that as little as 25% reduction in $Cdc42_{COR}$ sufficed to segregate WT-EC and *Cdc42*-KO-EC horizontally (Fig. S7E, Movie 24); however, $Cdc42_{COR}$ defects failed to reproduce the vertical segregation, and co-modulation with filopodia ($Cdc42_{FIL/COR}$) did not decrease the threshold of $Cdc42_{COR}$ required to match the *in vivo* data (Fig. S7F). $Cdc42_{ADH}$ simulations predicted that a substantially increased adhesion (2- to 2.75-fold) would be required to match the *in vivo* horizontal segregation data (Fig. S7G, Movie 25). However, simultaneous modulation of adhesion and filopodia ($Cdc42_{FIL/ADH}$) failed to show an additive effect (Fig. S7H), overall indicating that adhesion changes might well contribute to the horizontal segregation of *Cdc42* KO cells but cannot account for all aspects of the sprouting phenotype in *Cdc42*$^{i\Delta E}$ retinas. We finally modeled all four entities in combination ($Cdc42_{FIL/POL/ADH/COR}$) (Fig. S7I, Movie 26) and were able to find parameters that could match the *in vivo* data; interestingly now, a reduction rather than increase in intercellular adhesion was required to match the *in vivo* data, and both the extension of cortical actin-dependent junctional protrusions and polarity sensing ability had to be only moderately reduced (10% and 30%, respectively).

Taken together, *in silico* modeling results therefore indicate that filopodia formation and EC axial polarity exert the major influences on angiogenic sprouting, with regulation of junctional actin and cell adhesion playing a lesser role.

Defective EC migration leads to capillary-venous malformations

Vascular malformations are considered a subgroup of vascular anomalies that differ from vascular tumors by their nonproliferative nature (Wassef et al., 2015). In order to clarify whether the vascular lesions in *Cdc42*$^{i\Delta E}$ retinas would classify as vascular malformations, we analyzed EC proliferation in detail. We used 5-ethynyl-2′-deoxyuridine (EdU) incorporation to visualize active DNA synthesis in combination with a marker for endothelial cell nuclei (ERG) in order to identify proliferating ECs unambiguously, and subsequently quantified the EdU/ERG double-positive cells. Consistent with previously published results (Ehling et al., 2013), our analysis revealed that in control mouse retinas, EC proliferation occurs predominantly in veins and capillaries (Fig. 9A-C). Importantly, we were unable to detect any increase in EC proliferation in *Cdc42*$^{i\Delta EC}$ retinas, irrespective of vessel type (artery, vein, capillary) or quantification method. Neither the amount of EdU/ERG double-positive cells, nor the amount of EdU-positive cells per vascular area, significantly changed in *Cdc42*$^{i\Delta EC}$ retinas (Fig. 9A-C). Because proliferation in the mouse retina is reported to peak at P5 (Franco et al., 2015), which is 2 days prior to our analysis, we wanted to ensure that we had not missed an earlier, transient expansion of *Cdc42*-KO-EC. However, at P5, we also failed to observe any significant increase in EC proliferation (Fig. S8A,B). In addition, the total amount of ECs (quantified as ERG-positive nuclei) per retina was not significantly increased in *Cdc42*$^{i\Delta EC}$ retinas at P5 or at P7 (Fig. 9D, Fig. S8C). In spite of this, we observed a threefold increase in EC density in *Cdc42*$^{i\Delta EC}$ veins (Fig. 9F), in accordance with the dense concentration of ECs in the vascular lesions (Figs 9E and 10A, white boxes). The most plausible explanation for the crowding of ECs in the capillary-venous area is therefore that the proliferating ECs fail to migrate and re-distribute in the vascular tree. In fact, the inability of *Cdc42*-KO-EC to redistribute within the retinal vessel network was strikingly obvious in low degree chimeras, where *Cdc42*-KO-EC cells adopt a rounded shape and accumulate in veins and capillaries but fail to distribute into the arterial network (Fig. 10B). Quantifications of YFP$^+$ cells in arteries and veins revealed that in *Cdc42*$^{i\Delta EC}$ retinas the probability of a recombinant cell to be found in arteries is below 20% as compared to 50% in controls (see Materials and Methods for details) (Fig. 10C). We next quantified YFP$^+$ cell distribution in the retinal vasculature by subdividing the vascular network of adjacent artery-vein pairs and their intervening capillary plexus in four equal quadrants, quantifying the relative amount of YFP$^+$ recombinant cells in each quadrant and plotting the data in rose plots (Fig. 10D;

Development (2018) 145, dev161182. doi:10.1242/dev.161182

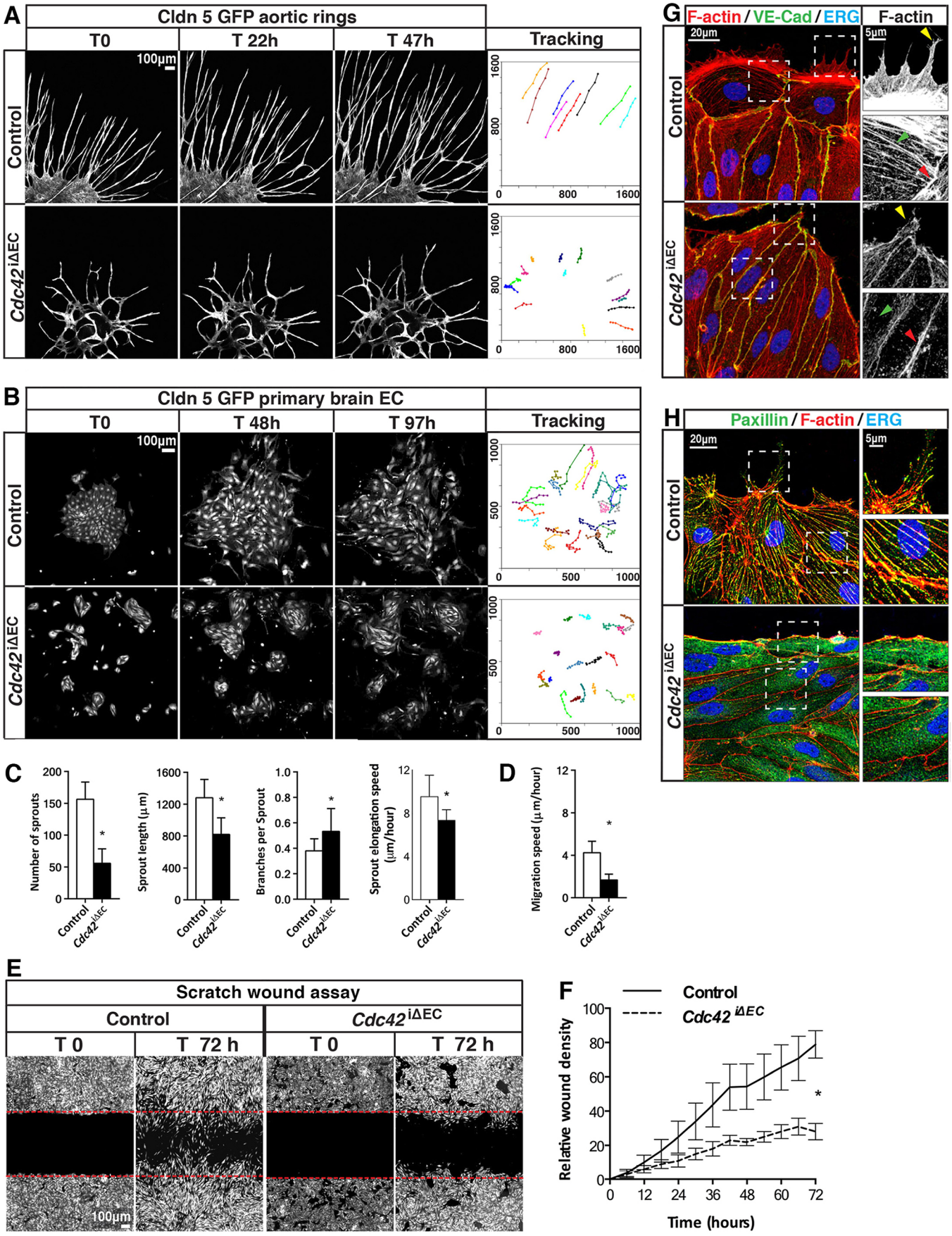

Fig. 7. See next page for legend.

Development (2018) 145, dev161182. doi:10.1242/dev.161182

Fig. 7. *Cdc42* is required for EC motility and directed cell migration. (A,B) Still images from time-lapse movies of aortic rings (A) (see also Movies 13 and 14) and primary brain ECs (B) (see also Movies 15 and 16) from Cldn5:GFP control and Cldn5:GFP *Cdc42*$^{i\Delta EC}$ mice at different time points (T, time in h). Right panels show tracking of individual cells. (C,D) Quantification of sprout number, length and branches per sprout in aortic explants from control (n=8 rings) and *Cdc42*$^{i\Delta EC}$ mice (n=10 rings), as well as of sprout elongation speed in aortic rings (C), and cell motility speed in primary brain ECs (control n=5 and *Cdc42*$^{i\Delta EC}$ n=5) (D); each containing >5-20 sprouts/cells analyzed (*P<0.05). (E) Still images from time-lapse movies showing scratch wound assays of confluent cell monolayers from Cldn5:GFP control and *Cdc42*$^{i\Delta EC}$ primary brain ECs isolated from P7 animals after 72 h. Red dashed lines denote scratch borders (see also Movies 17 and 18). (F) Quantification of relative wound density over time in scratch wound assay of primary brain ECs (control n=6; *Cdc42*$^{i\Delta EC}$ n=3). Two-way analysis of variance (ANOVA) repeated measures test was applied for statistical analysis; *P≤0.05). (G,H) Confocal images of primary brain ECs from P7 control and *Cdc42*$^{i\Delta EC}$ mice stained for F-actin (phalloidin), VE-cadherin, paxillin and ERG. Stress fibers (green arrowheads), junctional actin bundles (red arrowheads) and cellular protrusions (yellow arrowheads) are indicated. Dashed boxes denote magnified areas shown in the rightmost panels. Graphs show mean±s.d. (unpaired two-tailed Student's *t*-test, *P≤0.05).

see Materials and Methods for details). This analysis demonstrates that *Cdc42*-KO-EC accumulate in the proximity of veins and the adjacent vascular plexus and fail to distribute away from these sites (Fig. 10E,F). Based on these observations, we propose that the vascular malformations in *Cdc42*$^{i\Delta EC}$ retinas arise as a consequence of defective cell migration, when ECs, proliferating at normal rates, are unable to re-distribute within the vascular network. Malformations hence remain restricted to capillaries and veins, vessel types in which proliferation is naturally high (but not increased by the loss of Cdc42) and are absent from arteries, where proliferation is naturally low. The defective cell migration leads, in the presence of naturally high proliferation rates, to dilations of veins and capillaries that ultimately progress into mulberry-like vascular malformations (Fig. 10G).

DISCUSSION

Cdc42-regulated functions in retinal endothelial cells

Cdc42 is known to regulate a multitude of cellular processes, but although some of its functions appear conserved in all cell types studied, others are cell-type specific. In this study, we aimed to clarify which cellular processes are regulated by Cdc42 in ECs *in vivo* and how these processes contribute to angiogenic sprouting and blood vessel morphogenesis. To avoid secondary systemic effects on vascular development, a notorious problem with embryonic gene deletion, we inactivated Cdc42 postnatally and studied its effects in the developing retinal vasculature. At this location, we found that Cdc42 regulates only a subset of its reported functions in ECs, namely filopodia formation (Barry et al., 2015; Fantin et al., 2015; Sakabe et al., 2017; Wakayama et al., 2015), adherence junction stability (Barry et al., 2015; Broman et al., 2006) and migration (Jin et al., 2013; Sakabe et al., 2017; Vitorino and Meyer, 2008; Wakayama et al., 2015). However, other known functions, including A-B polarization, lumen formation and proliferation, did not appear to be significantly changed by the loss of Cdc42. That vascular lumens can form in *Cdc42*$^{i\Delta EC}$ retinas is surprising because Cdc42 has previously been implicated in vessel lumen formation both *in vitro* (Bayless and Davis, 2002; Davis et al., 2011) and during embryonic development (Barry et al., 2015). It is presently unknown whether the differences between embryonic and postnatal Cdc42 deletion reflect different requirements for Cdc42 in vascular lumen formation in embryonic and postnatal vessels. Because vascular lumens appear variably collapsed and dilated in Cdc42 mutant embryos (Barry et al., 2015), it is possible that these defects represent secondary consequences of cardiovascular dysfunction rather than primary defects in lumen formation. Differences in blood flow might also contribute to the observed differences. The mouse retinal vasculature develops by angiogenic sprouting from pre-existing lumenized vessels. The process of extension of the endothelial lumen during angiogenic sprouting involving inverse membrane blebbing dependent on blood pressure (Gebala et al., 2016). This differs from the proposed mechanism of endothelial lumen formation during vasculogenic vessel assembly in the aorta and yolk sac (Strilić et al., 2009, 2010), and *in vitro*, which takes place in the absence of blood flow. Consistent with our results, Barry and colleagues also observed that retinal blood vessels were lumenized following Cdc42 deletion and suggested that the timing of deletion relative to EC lumen formation might account for the presence of lumens and variability of phenotypes (Barry et al., 2015). Further studies are required to clarify the role of Cdc42 in vascular lumen formation in more detail.

Cdc42 is considered a key regulator of cell polarity (Etienne-Manneville, 2004). It is crucial for A-B polarization of epithelial cells *in vitro* (Bryant et al., 2010; Martín-Belmonte et al., 2007) and its deletion causes defects in lung (Wan et al., 2013), kidney (Elias et al., 2015) and pancreatic (Kesavan et al., 2009) tubular patterning owing to defective A-B polarization of the respective epithelia. Cdc42 has also been suggested to control A-B polarity in the endothelium (Barry et al., 2015; Lizama and Zovein, 2013), and, in addition, Cdc42 has been shown to control yet another aspect of cell polarity, PCP, both in the neuroepithelium of the inner ear (Kirjavainen et al., 2015) and during convergent extension in *Xenopus laevis* (Choi and Han, 2002). Surprisingly, our data indicate that in the postnatal retina, Cdc42 is dispensable for A-B polarization of blood vessels, but is essential for EC axial polarity in veins and capillaries. Our modeling data suggest that defective EC axial polarity affects the directional migration of tip cells at the sprouting front, as well as on stalk cells during sprout elongation and vascular regression. In agreement with a role of EC axial polarity in angiogenic sprouting, Dubrac and colleagues recently reported similar polarity defects upon EC-specific deletion of NCK1/2 (Dubrac et al., 2016). However, those polarity defects were only observed at the sprouting front and were not associated with vascular malformations. In *Cdc42*$^{i\Delta EC}$ retinas, the loss of axial polarity correlates with the formation of vascular malformations, but whether these phenomena are causally linked remains to be established.

Defective EC migration causes vascular malformation

We propose that defective EC migration is causal in the development of vascular malformations in *Cdc42*$^{i\Delta EC}$ retinas. Analysis of mosaic *Cdc42*$^{i\Delta EC}$ retinas showed that *Cdc42*-KO-EC were unable to disperse through the retinal vasculature and instead accumulated in veins and their adjacent capillaries. During retinal development, the naturally high EC proliferation in veins and capillaries generates new ECs, which, under normal conditions, get incorporated into the expanding vascular network. Because EC proliferation was unaffected in *Cdc42*$^{i\Delta EC}$ retinas, we conclude that the malformations build up when *Cdc42*-KO-EC are unable to migrate away from the location in which they are born. The inability of *Cdc42*-KO-EC to disperse within the vascular network explains their underrepresentation in arteries, and explains why arteries appear morphologically normal in *Cdc42*$^{i\Delta EC}$ retinas. Whereas defective cell migration alone might be predicted to cause local crowding of ECs, the formation of large, hollow and mulberry-shaped malformations likely depends on the

Development (2018) 145, dev161182. doi:10.1242/dev.161182

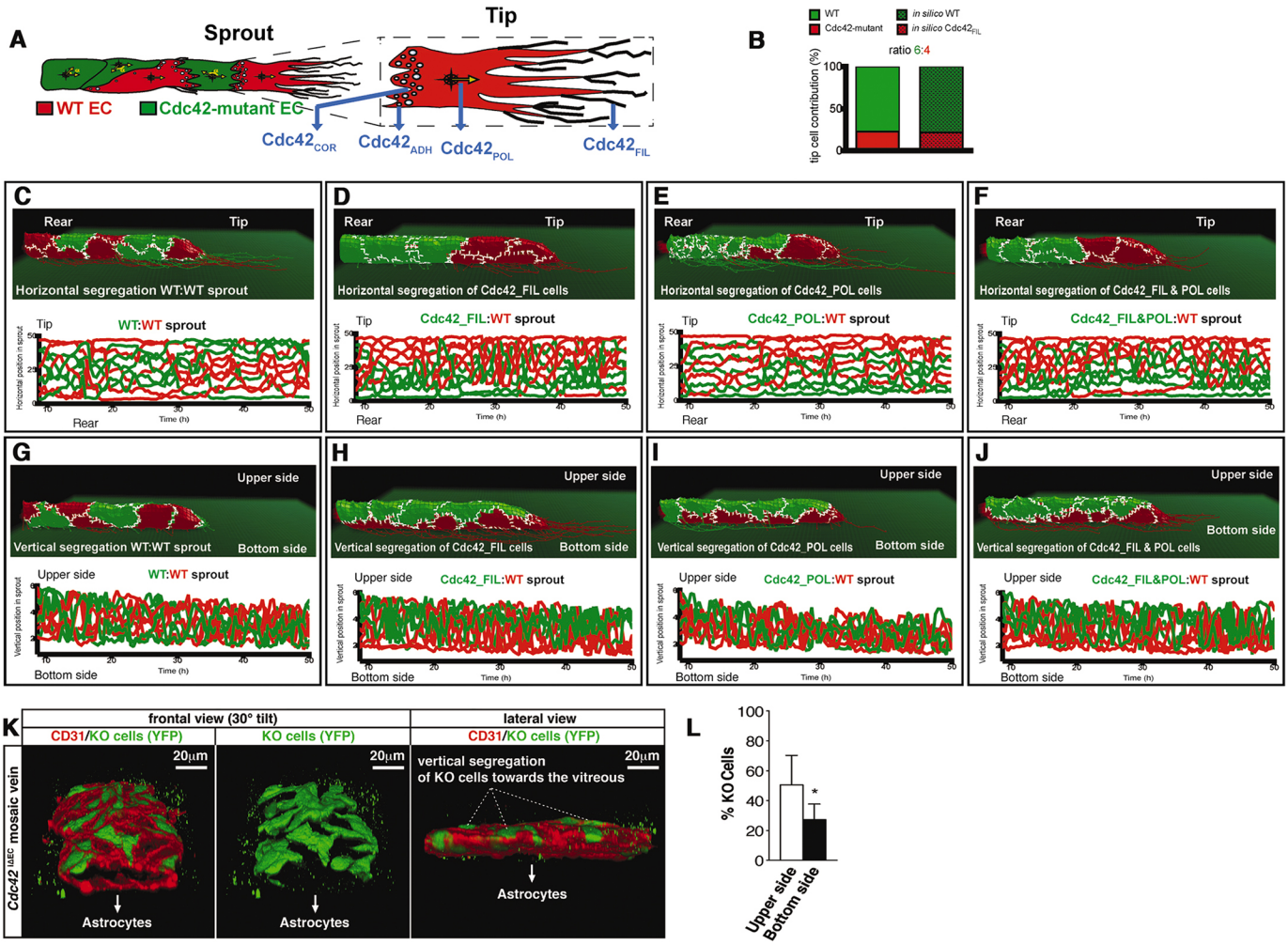

Fig. 8. Computational modeling of the different Cdc42-driven cellular processes affecting angiogenic sprouting. (A) Cartoon illustrating the different effectors modified, alone or in combination to simulate the *Cdc42*$^{i\Delta EC}$ phenotype-junctional actin ($Cdc42_{COR}$), intercellular adhesion ($Cdc42_{ADH}$), polarity ($Cdc42_{POL}$) and filopodia ($Cdc42_{FIL}$). White dots and yellow arrows represent VE-cadherin endocytosis and polarity-dependent directional movement, respectively, of simulated *Cdc42*-KO-EC (green) and WT-EC (red) in a sprouting vessel. (B) Quantification of *Cdc42*-KO-EC contribution to tip position (%) for experimental and simulated ($Cdc42_{FIL}$) vessels using a 6:4 ratio (*Cdc42*$^{i\Delta EC}$:WT). (C) Cell rearrangement in a control, *in silico* 1:1 WT:WT sprout (half WT cells green, half red). Green layer underneath the sprout represents the VEGF protein gradient. Kymographs depict the horizontal (tip to rear) movement of the green and red cells over time. Each intersection represents cells interchanging position, i.e. cell rearrangement. (D-F) memAgent-Spring model (MSM)-Cellular Potts model (CPM) representative screenshots showing the horizontal arrangement of *Cdc42*-KO-EC (green) and WT-EC (red) as viewed from above the vessel. Kymographs depict the tip to rear movement of *Cdc42*-KO-EC (green) and WT-EC (red) cells over time. (G-J) Vertical (top to bottom) movement of cells in the sprout over time with sprouts viewed from the side in screenshots. (K) 3D images of a confocal stack, showing a partially recombined vein of a P7 retina in *Cdc42*$^{i\Delta EC}$ mice. Green indicates *Cdc42*-KO-EC and red outlines the blood vessels (CD31 staining). (L) Quantification of *Cdc42*-KO-EC (%) cells situated in the upper (towards vitreous) and bottom side (towards astrocytes) of a mosaic vein (n=2 animals, 370 cells analyzed). Graphs show mean±s.d. (unpaired two-tailed Student's t-test, *$P \leq 0.05$).

naturally high EC proliferation at these sites. In keeping with this scenario, the vascular malformations in *Cdc42*$^{i\Delta EC}$ retinas were aggravated by pharmacological inhibition of Notch protein signaling, which is known to enhance EC proliferation. In conclusion, our results suggest that a balance between EC proliferation and migration is crucial for normal vascular morphogenesis and that a disturbance in this balance might provoke the formation of vascular malformations. Our data are also consistent with the idea that arteries form from vein-derived tip cells (Xu et al., 2014).

An interesting link between Cdc42 and the Hippo signaling pathway has recently been described in the context of tip cell migration and angiogenic sprouting (Sakabe et al., 2017; Kim et al., 2017). Whether Hippo signaling is of relevance for vascular malformations remains to be elucidated, however. It is further worth noting that the vascular malformations in *Cdc42*$^{i\Delta EC}$ retinas resemble those observed in animal models of cerebral cavernous malformations (CCMs), both in terms of lesion morphology and location (Boulday et al., 2011). Further studies should therefore investigate putative molecular similarities between *Cdc42*$^{i\Delta EC}$-induced malformations and CCMs.

MATERIALS AND METHODS

Ethical statement and mice

Animal housing, as well as the experiments performed, were in accordance with Swedish legislation and were approved by the local animal ethics committees prior to experimentation. The protocols included in this study were approved by the Stockholm's North Committee on the Ethics of Animal Experiments (permit number N33/10) and by the Uppsala Committee (permit numbers C224/12, C115/15, C111515/16). All efforts were made to minimize animal suffering. Mice were used regardless of their sex, because no difference in the phenotypes was detected.

Development (2018) 145, dev161182. doi:10.1242/dev.161182

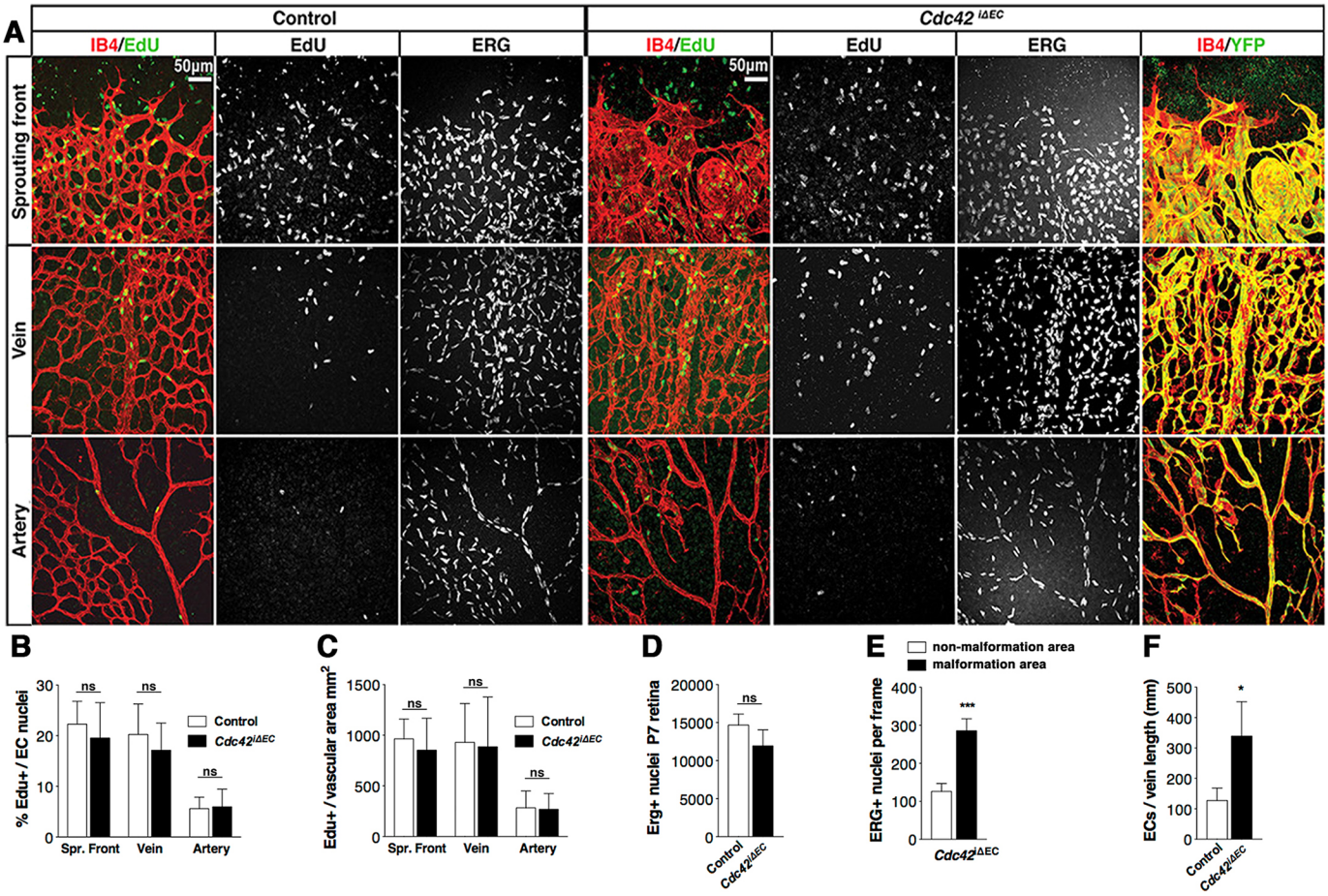

Fig. 9. EC proliferation is not altered in *Cdc42*$^{i\Delta EC}$ retinas. (A) Confocal images from P7 control and *Cdc42*$^{i\Delta EC}$ retinas stained for ECs (IB4), proliferating cells (EdU), recombination (YFP), and EC nuclei (ERG). Proliferation of ECs was analyzed in the sprouting front, veins and arteries 4 h after EdU administration into the pups. (B,C) Quantification of EC proliferation at P7 in the sprouting front (n=7), veins (n=6) and arteries (n=5), displayed as % of proliferating (EdU$^+$) cells per EC nuclei (B), or proliferating (EdU$^+$) cells per vascular area (C). (D) Total number of EC (ERG$^+$) in control (n=4) and *Cdc42*$^{i\Delta EC}$ (n=5) retinas at P7. (E) Quantification of EC density in malformed and nonmalformed vascular areas of *Cdc42*$^{i\Delta EC}$ retinas at P7 (n=9 frames per group); ***P<0.001. (F) Quantification of EC per vein length (mm) in control (n=8 veins) and *Cdc42*$^{i\Delta EC}$ (n=9 veins) retinas at P7 from three independent litters per group. Graphs show mean±s.d. (unpaired two-tailed Student's t-test; ns, nonsignificant; *P≤0.05).

Cdc42 KO and reporter mice

Endothelium-specific tamoxifen-inducible Cdc42 KO mice (referred to as *Cdc42*$^{i\Delta EC}$) were obtained by crossing *Cdc42*$^{flox/flox}$ mice (Wu et al., 2006) with endothelial-specific *Cdh5(PAC)-Cre*^{ERT2} mice (Pitulescu et al., 2010). To evaluate Cre-mediated recombination efficiency, *Cdc42*$^{i\Delta EC}$ mice were bred to *Rosa26-EYFP* (Srinivas et al., 2001) or, in a few cases, to *Rosa26-tdTomato(Ai14)* (Madisen et al., 2010) reporter mice. For all relevant experiments, *Cdh5(PAC)-Cre*^{ERT2}*:R26R-EYFP* and *Cdh5(PAC)-Cre*^{ERT2}*:R26-tdTomato* mice were used as controls. Postnatal gene deletion/reporter gene activation was induced by daily tamoxifen (T5648, Sigma-Aldrich) administration [100 µl of a 20 mg/ml solution in 90% corn oil (C8267, Sigma-Aldrich) and 10% ethanol], which was gavaged to lactating females from P0-P2 and transferred to the offspring through the milk. Mice were sacrificed for analysis at P7, unless otherwise noted. A technical note on the mosaic analysis: it should be highlighted that this approach relies on equal recombination efficiencies at the reporter locus and the *Cdc42*^{flox} locus and that, in principle, both constructs can recombine independently of one another. What we observe in practice is a high degree of correlation between reporter gene expression and a cell-autonomous phenotype (the loss of tip cell filopodia), which strongly argues for similar recombination rates. We analyzed a total of 239 YFP$^+$ 238 YFP$^-$ ECs at the tip cell position in ten highly recombinant *Cdc42*$^{i\Delta EC}$ retinas and found that only 2% of YFP$^+$ cells were able to extend filopodia, while 98% failed to do so. In contrast, 94% YFP$^-$ ECs at the tip cell position extended filopodia, whereas in the remaining 6% of YFP$^-$ ECs, filopodia formation appeared affected.

Cldn5(BAC)-eGFP mice

The transgenic mouse *Cldn5(BAC)-eGFP* (referred to as Cldn5:GFP), expressing eGFP under the control of the *Cldn5* promoter, was generated using bacterial artificial chromosome (BAC) technology. Further characterization of this transgenic line will be presented in a dedicated independent publication. Cldn5:GFP mice were bred into the *Cdc42*$^{i\Delta EC}$ or C57BL6J control WT backgrounds and used to unambiguously identify ECs in live imaging experiments.

Antibodies

For immunofluorescence in retinas and cells, the following antibodies were used (species, antibody, catalogue number, batch number, supplier, dilution): rat anti-VE-cadherin (14144181, E04063-1267, e-bioscience, 1:100); rat anti-ICAM2 (553326, 3308761, BD Biosciences, 1:200); goat anti-podocalyxin (AF15556, R&D Systems, 1:200); rabbit anti-collagen IV (2150-1470, 161115, AbD Serotec, 1:200); goat anti-CD31 (AF3628, R&D Systems, 1:500); rabbit anti-Golph4 (Golim4) (Ab28049, GR244016-7, Abcam, 1:400); rabbit anti- ERG (92513, GR219881-25, Abcam, 1:200); chicken anti-GFP (13970, GR236651-21, Abcam, 1:500); rabbit anti-cleaved caspase 3 (9661, 9661S, Cell Signaling Technology, 1:400); mouse anti-GM130 (Golga2) (610823, Transduction, 1:400); goat anti-VE-cadherin (sc-6458, A1912, Santa Cruz Biotechnology, 1:400); mouse anti-β-catenin (610154, 64266, BD Pharmingen, 1:400); mouse anti-paxillin (610051, 3053935, BD Biosciences, 1:400); rabbit anti-ZO-1 (40-2300, 977576A, Invitrogen, 1:400), rabbit anti-aPKCζ (sc-216, K0113,

Development (2018) 145, dev161182. doi:10.1242/dev.161182

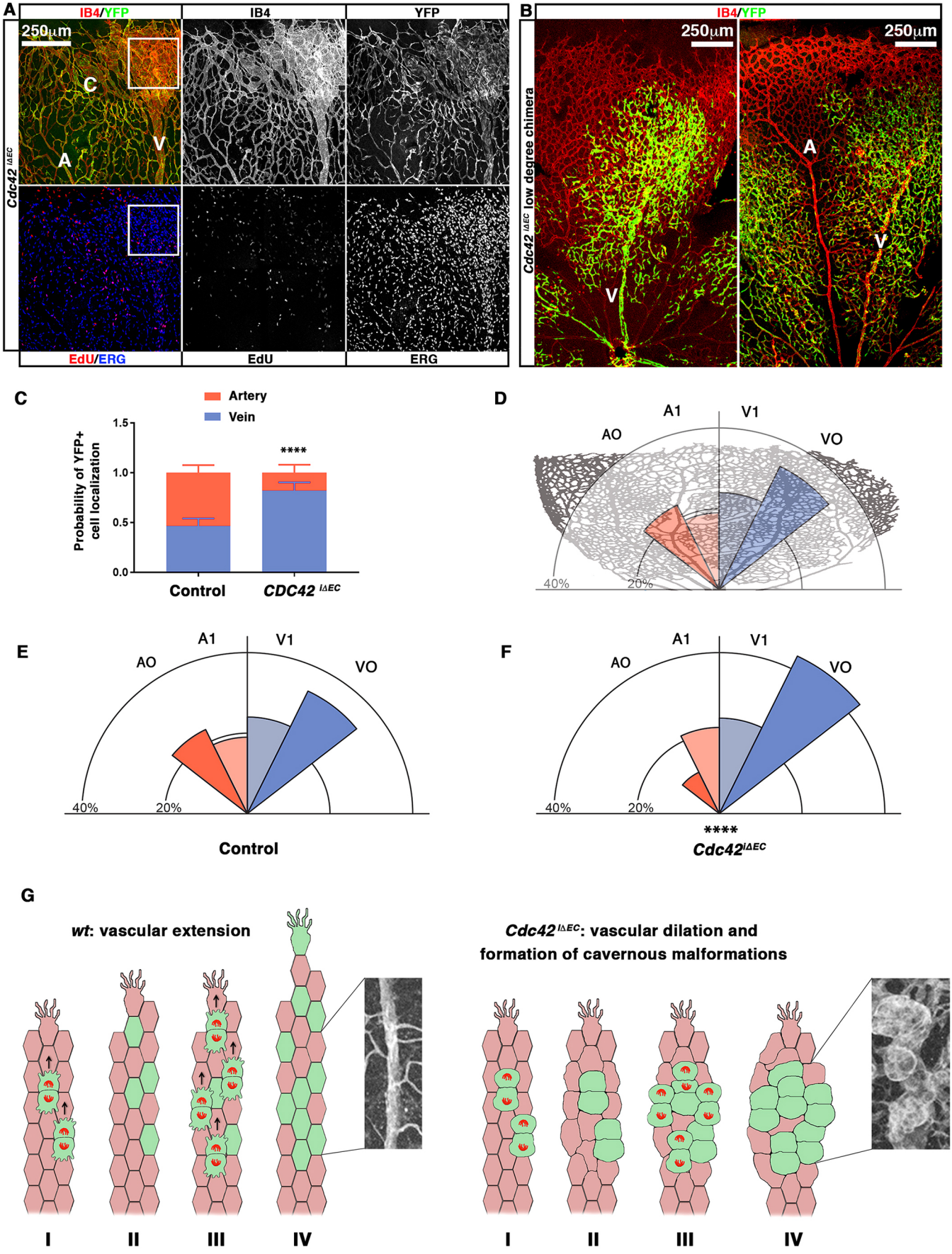

Fig. 10. See next page for legend.

Development (2018) 145, dev161182. doi:10.1242/dev.161182

Fig. 10. Defective EC migration leads to vascular malformations.
(A) Confocal image of a typical malformation in a *Cdc42*$^{i\Delta EC}$ retina. Veins (V), capillaries (C), and arteries (A) are indicated. Immunostaining indicates ECs (IB4), EC nuclei (ERG), proliferating cells (EdU) and recombination (YFP). The boxed areas highlight a venous malformation, in which EC nuclei are densely packed although proliferation is not increased. (B) Confocal images of P7 low degree chimera *Cdc42*$^{i\Delta EC}$ retinas stained for EC (IB4) and recombination (YFP). Note that YFP$^+$ ECs (*Cdc42*-KO-EC) remain in the vicinity of veins (V) and that arteries (A) are deprived of YFP$^+$ ECs. (C) Quantification of the probability of YFP$^+$ cell localization (control n=4 retinas, 13 artery-vein pairs; *Cdc42*$^{i\Delta EC}$ n=3 retinas, 12 artery-vein pairs) calculated as percentage of YFP recombination in a vessel over percentage of YFP recombination in an artery-vein pair (graph shows mean±s.d. (two-way ANOVA; ****P<0.0001).
(D) Schematic illustration of quadrant-based YFP distribution analysis in a retinal wedge: quadrants are labeled from A0 (most proximal to the artery) to V0 (most proximal to the vein). (E,F) Rose diagrams showing the quadrant-based YFP distribution in control retinas (n=3, six wedges) (E) and *Cdc42*$^{i\Delta EC}$ retinas (n=3, six wedges) (F) (****P<0.0001). (G) Schematic illustration of EC dispersion in control (left) and *Cdc42*$^{i\Delta EC}$ (right) veins, proliferating at similar rates, represented in four stages (I-IV). In WT veins, EC proliferation is balanced by local EC re-arrangements and EC migration, leading to vessel extension (representative confocal image on the right). In *Cdc42*$^{i\Delta EC}$ veins, vascular malformations arise when ECs, proliferating at normal rates, fail to re-distribute in the vascular tree (representative image on the right). Values indicate mean±s.d.

Santa Cruz Biotechnology, 1:400), rabbit anti-Par3 (07-330, DAM1772423, Millipore, 1:400). Phalloidin-488 (PK-PF488P-7-01, 357P039, PromoKine, 1:200) and phalloidin-555 (PK-PF555-7-01, 370P054, PromoKine 1:200) were also used, and, in some cases, nuclei were labeled with Hoechst 33342 (Invitrogen) diluted 1:10,000 in phosphate-buffered saline (PBS).

Retinal immunohistochemistry

Whole-mount staining of retinas was performed as previously described (Gerhardt et al., 2003). In brief, eyes were fixed in 4% paraformaldehyde (PFA) in PBS at 4°C (1-2 h), retinas were dissected and permeabilized in PBS, 1% bovine serum albumin (BSA), and 0.5% Triton X-100 at 4°C overnight. For isolectin B4 (IB4) staining, retinas were permeabilized in PBlec (PBS, pH 6.8, 1% Triton-X100, 0.1 mM $CaCl_2$, 0.1 mM $MgCl_2$, 0.1 mM $MnCl_2$) and incubated with IB4, Alexa Fluor 647 conjugate (I32450, Life Technologies) in PBlec at 4°C overnight. Primary antibodies were diluted in PBS, 0.5% BSA and 0.25% Triton X-100 and incubated at 4°C from 4 h to overnight depending on the sample, followed by detection with secondary antibodies (Alexa Fluor 405, 488, 568, Cy3 or 647, Life Technologies). Retinas were mounted using ProLong Gold Antifade (Life Technologies).

Confocal microscopy and image processing

Images were acquired using a Leica SP8 confocal microscope. Maximum intensity projections and 3D reconstructions of serial Z-sections were generated using LAS AF software (Leica Microsystems). Image processing and quantification was performed with Volocity 6.3 (Improvision) or Fiji (NIH). Figures were assembled using Adobe Photoshop and Illustrator CS6. Genotypes and treatments were blinded for all analyses.

Filopodia and apoptosis quantification

Confocal images of whole-mount retinas, were taken using different objectives. For filopodia quantification, images were acquired with an HC PL APO 63×/1.30 GLYC objective and quantified in six fields/retina (two arterial front fields, two venous front fields and two front fields in between the artery and vein). Total number and filopodia length from WT and Cdc42 KO endothelial tip cells were quantified. For apoptosis analysis, cleaved caspase 3 staining from nine fields per animal was acquired using an HC PL APO 40×/1.10 W objective (three arterial fields, three venous fields and three fields between the artery and vein). The total number of double-positive cells (cleaved caspase 3$^+$ and IB4$^+$ or CD31$^+$) per field was analyzed.

Tip cell disadvantage calculation

The overall recombination rate in P5 and P7 retinas, referred to as SR, was calculated as the percentage of YFP$^+$ vascular area (YFP$^+$/IB4 or CD31 area ×100) The maximum intensity projected confocal images of the whole retina wedges were acquired with an HC PL APO 10×/0.4 CS objective. TR was calculated as the percentage of recombined tip cells (number YFP$^+$/total number of tip cells ×100) using sprouting front pictures taken with HC PL APO 40×/1.10 W and HC PL APO 63×/1.30 GLYC objectives. TR/SR ratios were quantified in the vascular front of retinas, with six fields/retina.

For aortic rings, maximum intensity projected confocal images of whole aortic explants from *Cldn5*:GFP$^+$ controls and *Cdc42*$^{i\Delta EC}$ were acquired with an HCX IRAPO L 25×/0.95 W 0.17 objective. SR and TR were quantified in six fields, considering tdTomato+area as the Cre recombination marker, and the Cldn5 GFP$^+$ area as the vessel marker.

Measurement of vascular extension, vessel length and width in retinas

Tile scans of flat-mounted retinas from control and *Cdc42*$^{i\Delta EC}$ mice were acquired using an HC PL APO 10×/0.4 CS objective on a Leica SP8 confocal microscope. Vascular extension, artery and vein length, as well as the widths of arteries, veins, and capillaries, were measured in at least three individual animals.

Analysis of cellular distribution in mosaic retinas

To determine the distribution of ECs within the retinal vasculature at P7, the location of YFP$^+$ cells was analyzed in low degree chimeras (between 7% and 52% recombination rate). The probability of ECs in *Cdc42*$^{i\Delta EC}$ localizing to an artery or a vein was analyzed and compared with control retinas [*Cdh5(PAC)-Cre*^{ERT2}; *Rosa26-EYFP*]. Retinas were stained with IB4 to visualize the entire vascular network and, in addition, with an antibody against GFP to visualize YFP$^+$ ECs. Four incisions were made in each retina in order to obtain four wedges each containing an artery-vein pair.

In order to analyze the probability of ECs localizing in arteries and veins, the percentage of YFP recombination was measured in adjacent arteries and veins (but not in the surrounding capillaries) and normalized to the total level of recombination in both vessels:

$$\text{Probability of YFP}^+\text{ cell artery} = \frac{\text{YFP}^+\text{ area artery}/\text{IB4}^+\text{ area artery}}{\text{YFP}^+\text{ area both vessels}/\text{IB4}^+\text{ area both vessels}}$$

$$\text{Probability of YFP}^+\text{ cell vein} = 1 - (\text{probability of YFP}^+\text{ cell in artery}).$$

Two-way ANOVA was performed to calculate statistical significance (13 artery-vein pairs were analyzed in four control retinas and 12 artery-vein pairs in three *Cdc42*$^{i\Delta EC}$ retinas). In order to determine the overall distribution of ECs within the retinal plexus, we subdivided the wedge containing an artery and vein into four longitudinal quadrants: the first quadrant (A0) contained an artery and included the capillary plexus proximal to the artery; the second quadrant (A1) contained the capillary plexus distal to the artery; the third quadrant (V1) contained the capillary plexus distal to the vein; and the fourth quadrant (V0) contained the vein and its proximal capillary network. YFP signal in each quadrant was quantified and normalized to the total YFP signal of the analyzed wedge:

$$\text{YFP}^+\text{ signal quadrant} = \frac{\text{YFP}^+\text{ area quadrant}}{\text{YFP}^+\text{ area wedge}}.$$

χ^2 test was used to compare the distribution of YFP$^+$ signal among the quadrants of the two groups (two artery-vein pairs and their adjacent capillary vasculature were analyzed per animal in three controls and three *Cdc42*$^{i\Delta EC}$ animals).

In vivo pharmacological inhibition of Notch protein signaling

Single injection of 0.1 mg/g gamma secretase inhibitor DAPT (565770, Calbiochem) dissolved in 10% ethanol and 90% corn oil (injection volume 10µl/g body weight) was administered subcutaneously to P7 controls and

Development (2018) 145, dev161182. doi:10.1242/dev.161182

Cdc42$^{i\Delta EC}$ mice for 12 h. Untreated *Cdc42*$^{i\Delta EC}$ and control mice injected with vehicle were used as experimental controls. Confocal images of three fields/retina were acquired using an HC PL APO 40×/1.10 W objective (one arterial front field, one venous front field and one front field between the artery and vein). Total number of filopodia per 100 µm of vascular front length was normalized to vehicle-treated control retinas.

Endothelial cell proliferation

Proliferation of ECs was examined using a Click-iT EdU Alexa Fluor 555 Imaging Kit (C10638, Invitrogen). EdU was prepared (5 mg/ml in 10% dimethyl sulfoxide) and 10 µl/g body weight was injected intraperitoneally into pups 4 h before sacrifice. Retinas were stained for ERG, GFP, and IB4 or CD31, and images were acquired with an HCX IRAPO L 25×/0.95 W 0.17 25× objective. Quantification of EC proliferation, displayed as percentage of proliferating (EdU$^+$) cells/per EC nuclei (ERG$^+$) and proliferating (EdU$^+$) cells per vascular area (scored as IB4$^+$ or CD31$^+$ area), was measured in whole retinas or in four pictures of sprouting front, four veins, and four arteries per retina.

EC quantification

Tile scan confocal images of whole-mount retinas were taken using an HCX IRAPO L 25×/0.95 W 0.17 objective. Retinas were stained for ERG, GFP and IB4 or CD31. Total number of ECs per retina (ERG$^+$ nuclei) was quantified in P5 (control n=3 and *Cdc42*$^{i\Delta EC}$ n=4) P7 retinas. Moreover, in P7 retinas, total number of ECs (ERG$^+$ nuclei) per vein length (mm) and EC density (ERG$^+$ nuclei per frame) was quantified in nine pictures (300 µm×300 µm) from malformed areas versus nonmalformed areas in *Cdc42*$^{i\Delta EC}$ retinas.

Aortic ring assay

Briefly, thoracic aortas were dissected from P7 Cldn5:GFP WT and Cldn5:GFP *Cdc42*$^{i\Delta EC}$ mice immediately after sacrifice. The fibro adipose tissue was removed and the aortas were serially cross-sectioned into 1- to 2-mm-thick rings. The aortic rings were embedded between two layers of collagen type I (1.5 mg/ml) (354236, BD Biosciences). The mouse aortic explants were then cultivated at 37°C, 5% CO_2 with Dulbecco's modified Eagle medium (DMEM) without Phenol Red (31053-028, Life Technologies) and supplemented with 15% fetal calf serum (Sigma-Aldrich), 30 ng/ml VEGF-A165 (450-32, PeproTech), 25 mM HEPES, 1.2 mM sodium pyruvate, penicillin (100 µg/µl) and streptomycin (100 µg/µl) using 24 glass bottom wells (P24G-1.5-13-F, MatTek). After 3-4 days of culture, when the aortic rings were sprouting, they were imaged over 2-3 days. After live imaging experiments, the aortic rings were fixed in 4% PFA. Confocal tile images of whole aortic explants were taken using an HC PL APO 10×/0.4 CS or HCX IRAPO L 25×/0.95 W 0.17 objective. Sprout number, length and branches per sprout in aortic explants from WT controls and *Cdc42*$^{i\Delta EC}$ were quantified.

Isolation, culture, immunohistochemistry and analysis of primary brain ECs

EC isolation was based on the method described in Niaudet et al. (2015). P7 brains from control and *Cdc42*$^{i\Delta EC}$ mice were minced and digested with 1% collagenase (C6885, Sigma-Aldrich) in HEPES-buffered DMEM (Life Technologies) for 10 min under stirring at 400 rpm and 37°C. The cell suspension was filtered through a 70-mm nylon strainer (BD Falcon) and collected by centrifugation at 300 ***g*** for 10 min. Cell pellets were resuspended in DMEM supplemented with 10% FBS and incubated for 45 min RT with Dynabeads (Invitrogen) previously coated with rat-anti mouse PECAM1 antibody (553370, BD Pharmingen). ECs were separated using a magnet bar and dissociation from the beads was carried out with Tryp-LE 10× (Life Technologies). Brain ECs were cultured at 37°C, 5% CO_2, in endothelial cell growth medium 2 (C22011, Promo Cell). For immunofluorescence, brain ECs in culture were fixed for 5 min in 3% PFA and permeabilized with 0.2% BSA, 0.1% Triton-X100 in PBS for 1 h. Primary antibodies were diluted in 0.1% BSA, 0.05% Triton X-100 in PBS and incubated for 2 h at room temperature, followed by 1 h incubation with secondary antibodies (Alexa Fluor 405, 488, 568, Cy3 or 647, Life Technologies). The effects of Cdc42 deletion on the actin cytoskeleton, EC junctions and mislocalization of paxillin, Par3 and aPKC, was consistently observed in at least three independent primary brain EC cultures and analyzed in at least 50 cells, in which ∼100% of cells were consistent with the reported phenotype.

Live imaging of aortic rings, primary brain ECs and cell tracking

Live imaging experiments were performed with primary brain ECs and aortic rings isolated from P7 Cldn5:GFP control and Cldn5:GFP, *Cdc42*$^{i\Delta EC}$ mice (tdTomato was used to report recombination in these experiments). Confocal microscope with motorized stage and incubation equipment (brick gas mixer, 5% CO_2 and temperature control at 37°C) was used to image the samples over 24-97 h using an HC PL APO 10x/0.4 CS or HCX IRAPO L 25×/0.95 W 0.17 objective. Tracking analysis was performed using the MTrackJ plugin from Fiji and expressed as migration speed (µm/h) for ECs and sprout elongation speed (µm/h) for aortic rings. Aortic ring and EC movies were created from the captured images using Fiji software.

In vitro scratch wound assay

Primary brain ECs isolated from P7 Cldn5:GFP controls and Cldn5:GFP, *Cdc42*$^{i\Delta EC}$ animals (tdTomato was used to report recombination in these experiments) were seeded in ImageLock 96-well plates (Essen Bioscience). Confluent cell monolayers were scratched using a 96-pin mechanical device (WoundMaker, Essen Bioscience), producing a 700-800 µm wound. Cell migration was recorded for 72 h using a 10× objective with IncuCyte ZOOM (Essen Bioscience). The integrated CellPlayer Cell Migration Software Module (Essen Bioscience) enabled automated analysis of IncuCyte cell migration, and relative wound density analysis was performed in multiple scratches from control and *Cdc42*$^{i\Delta EC}$ cultures. Two-way analysis of variance (ANOVA) repeated measures test was applied for statistical analysis. The overall recombination rate (80.8±12.02%) in scratch assay was calculated in three animals from three independent experiments as the percentage of Ai14 (tdTomato)-positive vascular area (Ai14$^+$/Cldn5$^+$ area ×100).

Endothelial axial polarity analysis

Following the scratch assay, brain ECs were stained for EC nuclei ERG, VE-cadherin, and the Golgi marker GM130. EC polarization towards the wound was determined by the nucleus-Golgi axis angle as previously described (Etienne-Manneville and Hall, 2001). A cell was considered correctly polarized when the Golgi apparatus was oriented within ±45° perpendicular to the wound border. To evaluate Golgi orientation in blood vessel *in vivo*, P7 retinas were stained with CD31, Golph4, and ERG or Hoechst. Confocal images from arteries, veins and capillaries at the sprouting front region were taken, and the orientation of EC nucleus-Golgi pairs along blood vessels was analyzed by optical sectioning (see Movie 12 for how polarity was determined and Table S1 for quantification details). The percentage of ECs with the Golgi polarized within ±45° against the predicted flow direction was determined in arteries and veins. For the sprouting front, the percentage of ECs in the first (tip), second and third (stalk) rows with the Golgi polarized ±45° towards the center and retinal periphery was determined. Rose plots showing the angular distribution of individual nucleus-Golgi orientation were generated in Oriana4 software (Kovach Computing).

Western blotting and qRT-PCR

Freshly isolated brain ECs from P7 control and *Cdc42*$^{i\Delta EC}$ animals were snap-frozen, lysed and used for western blotting and qRT-PCR. Proteins from frozen cells were extracted in phospho-lysis buffer (50 mM Tris-HCl pH 7.5, 150 mM NaCl, 0.5% deoxycholate, 0.5% SDS, 0.1% NP-40, 0.1% Triton X-100, supplemented with PhosSTOP phosphatase inhibitor and Complete protease inhibitor cocktail (both Roche Diagnostics).

Ten micrograms of total proteins were separated by sodium dodecyl sulfate polyacrylamide gel electrophoresis on 4-12% gradient gels (Bio-Rad) and transferred to polyvinylidene fluoride membranes (Immobilon-P, Millipore). Membranes were incubated with primary antibodies rabbit anti-Cdc42 (2466, Cell Signaling Technology) and anti-calnexin (ab22595, Abcam), followed by horseradish peroxidase-linked secondary antibodies, and signals were detected by a chemiluminescence system (GE Healthcare).

Total RNA was isolated using an RNeasy micro kit (Qiagen). Reverse transcription was performed using iScript Reverse Transcription Supermix (Bio-Rad). cDNA was amplified in a CFX96 Real-Time system (Bio-Rad)

Development (2018) 145, dev161182. doi:10.1242/dev.161182

using Taqman probe *Cdc42* (Mm01194005). Expression levels were normalized to the housekeeping gene encoding for *Gapdh*. Fold change differences were calculated based on the relative quantification C_T method, also referred as $2^{-\Delta\Delta CT}$.

Computational modeling

The memAgent-Spring model (MSM) of tip/stalk dynamics in angiogenesis was used (see Bentley et al., 2008, 2009 for full details of methods). In the MSM, the EC membrane is represented by a collection of computational agents ('memAgents'), permitting localized responses of the cell to its environment. These memAgents are connected by springs following Hooke's law, capturing the tension in the actin cortex beneath. The model is well calibrated to match *in vivo* and *in vitro* VEGF/Dll4/Notch protein signaling and cell shape changes during filopodia-led cell migration and has been experimentally verified (Bentley and Chakravartula, 2017; Kur et al., 2016; Ubezio et al., 2016).

For simulations involving cell rearrangement, the *in vivo*-validated MSM-Cellular Potts model (CPM) model was utilized (see Bentley et al., 2014a for full methods), which was previously calibrated to *in vitro* sprouting data. This model integrates a Cellular Potts module to simulate local junctional dynamics as cells rearrange in the adhered tube, encompassing differential adhesion-based mechanisms.

We evaluated each Cdc42 cellular process alone (filopodia, adhesion, actin cortex and polarity) or in combination (Fig. 8A) in simulated vessels consisting of randomly positioned *Cdc42*-KO-ECs and WT-ECs in a (6:4) ratio matching our *in vivo* ratio, and compared those with simulations of WT:WT. ECs (Fig. 8C, Movie 19). To model each simulated cellular effector of Cdc42 alone (filopodia, polarity, junctional actin cortex and intercellular adhesion), an existing parameter of the MSM-CPM was changed with a constant k as described below (Fig. 8A). We conducted a sensitivity analysis over a range of values for k (for all processes except filopodia, where the reduction had been quantified *in vivo*, in which case k was calibrated to match this reduction) to find how much of a reduction, if any, is required in that particular process to match the *in vivo* contribution of KO cells to the tip and what other phenotypic effects would be predicted.

(1) $Cdc42_{FIL}$: modulating the probability of filopodia extension

$$P\ (\text{filopodia}) = C + k_1.$$

By simulating negative k_1-values, the cells' ability to extend filopodia is reduced. We first calibrated the MSM-CPM to the reduced filopodia number observed *in vivo* (Fig. S7A). This led to a decrease in filopodial lengths in subsequent simulations, matching the *in vivo* data with good accuracy (Fig. S7B).

(2) $Cdc42_{POL}$: modulating polarized formation of junctional cortex protrusions.

To simulate a polarity loss mutant, a new threshold k_2 was added to the polarity-sensing module of the MSM-CPM. By stochastic generation of a random number ρ, we allowed any copyflip attempt, by which an *in silico* EC protrudes its junctional cortex into a neighboring EC's space, to take place if $\rho \geq k_2$. However, if $\rho < k_2$, copyflips were only allowed to occur when they were polarized towards the tip of the sprout (as described in Bentley et al., 2014a). For example, a k2-value of 0.50 increases the chance of accepting a nonpolarized copyflip with 50% (whereas these are not accepted at all in the original MSM-CPM).

(3) $Cdc42_{COR}$: modulating the probability of junctional cortex protrusion formation

$$P\ (\text{junctional protrusion}) = \left[1 - \frac{N}{\left(\frac{N_{tot}}{\lambda}\right)}\right] + k_3.$$

By simulating negative k_3 values, the cells' ability to form junctional protrusions, which facilitate cell movement, is reduced.

(4) $Cdc42_{ADH}$: modulating the cellular adhesion levels

$$\eta = \eta + k_4.$$

By simulating negative or positive k_4 values, a cell is respectively made more weakly or strongly adhesive.

In vivo vertical segregation analysis

P7 $Cdc42^{i\Delta EC}$ retinas were stained with CD31 and GFP, to visualized recombined cells. 3D images of confocal stacks from veins were acquired, and quantification of the percentage of *Cdc42*-KO-EC (YFP^+) cells situated in the upper (towards the vitreous) and bottom side (towards astrocytes) of $Cdc42^{i\Delta EC}$ veins was analyzed (n=2 animals, 370 cells analyzed).

Statistical analysis

Statistical significance was determined by performing a number of analyses; unless otherwise stated, unpaired two-tailed Student's t-test was used. One-way ANOVA, two-way ANOVA and χ^2 test were performed where appropriate (see each experimental method for details). GraphPad Prism version 7.02 for Windows (GraphPad Software) was used for the analyses. Differences were considered significant with a P-value <0.05. The variance was similar between the groups that were statistically compared and their distribution was normal. Quantified data are presented as bar graphs of mean±s.d., shown as error bars or as rose diagrams of the mean.

Acknowledgements

We thank Pia Peterson, Jana Chmielniakova, Cecilia Olsson, Helen Leksell for technical assistance; Thommie Karlsson for help with microscopy; and Jennifer Hofmann and Lena Claesson-Welsh for critical reading of the manuscript.

Competing interests

The authors declare no competing or financial interests.

Author contributions

Conceptualization: B.L., M.C., C. Betsholtz, K.G.; Methodology: B.L., M.C., C.N., K.B., K.G.; Validation: B.L., M.C., C.N., K.B., B.C., K.G.; Formal analysis: B.L., M.C., B.C., A.A.-A., K.B., K.G.; Investigation: B.L., M.C., B.C., K.B., C.N., K.G.; Resources: K.B., C. Brakebusch, C. Betsholtz; Writing - original draft: B.L., M.C., K.B., K.G.; Writing - review & editing: B.L., M.C., C.N., A.A.-A., K.B., C. Betsholtz, K.G.; Visualization: B.L., M.C., C.N., K.B., K.G.; Supervision: P.C.,K.B., B.L., C. Betsholtz, K.G.; Project administration: C. Betsholtz, K.G.; Funding acquisition: K.B., P.C., C. Betsholtz.

Funding

This work was supported by the Swedish Cancer Foundation [CAN2015/771 to C. Betsholtz], Vetenskapsrådet [VR2015-00550 to C. Betsholtz], the European Research Council [2011-294556 to C. Betsholtz; EU-ERC269073 to P.C], Knut och Alice Wallenbergs Stiftelse [2012.0272 to C. Betsholtz and K.B.], Fondation Leducq [14-CVD-02 to C. Betsholtz and K.G.], FP7 People: Marie-Curie Actions [317250 to M.C.], the Wenner-Gren Foundation [to C. Betsholtz and K.G.], the Ministerio de Educación, Cultura y Deporte [EDU/2934/2009 to B.L.], Longterm Structural Funding – Methusalem Funding by the Flemish Government [to P.C.], Federaal Wetenschapsbeleid [IUAP grant P7/03 to P.C.], Agentschap voor Innovatie door Wetenschap en Technologie [PhD fellowship to B.C.], and Sundhed og Sygdom, Det Frie Forskningsråd [to C. Brakebusch].

Supplementary information

Supplementary information available online at
http://dev.biologists.org/lookup/doi/10.1242/dev.161182.supplemental

References

Abu Taha, A. and Schnittler, H.-J. (2014). Dynamics between actin and the VE-cadherin/catenin complex: novel aspects of the ARP2/3 complex in regulation of endothelial junctions. *Cell Adh. Migr.* **8**, 125-135.

Barry, D. M., Xu, K., Meadows, S. M., Zheng, Y., Norden, P. R., Davis, G. E. and Cleaver, O. (2015). Cdc42 is required for cytoskeletal support of endothelial cell adhesion during blood vessel formation. *Development* **42**, 3058-3070.

Bayless, K. J. and Davis, G. E. (2002). The Cdc42 and Rac1 GTPases are required for capillary lumen formation in three-dimensional extracellular matrices. *J. Cell. Sci.* **115**, 1123-1136.

Bentley, K. and Chakravartula, S. (2017). The temporal basis of angiogenesis. *Philos. Trans. R. Soc. Lond., B Biol. Sci.* **372**, 20150522.

Bentley, K., Gerhardt, H. and Bates, P. A. (2008). Agent-based simulation of notch-mediated tip cell selection in angiogenic sprout initialisation. *J. Theor. Biol.* **250**, 25-36.

Bentley, K., Mariggi, G., Gerhardt, H. and Bates, P. A. (2009). Tipping the balance: robustness of tip cell selection, migration and fusion in angiogenesis. *PLoS Comput. Biol.* **5**, e1000549.

Bentley, K., Franco, C. A., Philippides, A., Blanco, R., Dierkes, M., Gebala, V., Stanchi, F., Jones, M., Aspalter, I. M., Cagna, G. et al. (2014a). The role of differential VE-cadherin dynamics in cell rearrangement during angiogenesis. *Nat. Cell Biol.* **16**, 309-321.

Bentley, K., Philippides, A. and Ravasz Regan, E. (2014b). Do endothelial cells dream of eclectic shape? *Dev. Cell* **29**, 146-158.

Boulday, G., Rudini, N., Maddaluno, L., Blécon, A., Arnould, M., Gaudric, A., Chapon, F., Adams, R. H., Dejana, E. and Tournier-Lasserve, E. (2011). Developmental timing of CCM2 loss influences cerebral cavernous malformations in mice. *J. Exp. Med.* **208**, 1835-1847.

Boureux, A., Vignal, E., Faure, S. and Fort, P. (2007). Evolution of the Rho family of ras-like GTPases in eukaryotes. *Mol. Biol. Evol.* **24**, 203-216.

Bradley, J. R., Thiru, S. and Pober, J. S. (1995). Hydrogen peroxide-induced endothelial retraction is accompanied by a loss of the normal spatial organization of endothelial cell adhesion molecules. *Am. J. Pathol.* **147**, 627-641.

Broman, M. T., Kouklis, P., Gao, X., Ramchandran, R., Neamu, R. F., Minshall, R. D. and Malik, A. B. (2006). Cdc42 regulates adherens junction stability and endothelial permeability by inducing alpha-catenin interaction with the vascular endothelial cadherin complex. *Circ. Res.* **98**, 73-80.

Bryant, D. M., Datta, A., Rodríguez-Fraticelli, A. E., Peränen, J., Martín-Belmonte, F. and Mostov, K. E. (2010). A molecular network for de novo generation of the apical surface and lumen. *Nat. Cell Biol.* **12**, 1035-1045.

Choi, S.-C. and Han, J.-K. (2002). Xenopus Cdc42 regulates convergent extension movements during gastrulation through Wnt/Ca2+ signaling pathway. *Dev. Biol.* **244**, 342-357.

Davis, G. E., Stratman, A. N., Sacharidou, A. and Koh, W. (2011). Molecular basis for endothelial lumen formation and tubulogenesis during vasculogenesis and angiogenic sprouting. *Int. Rev. Cell Mol. Biol.* **288**, 101-165.

De Smet, F., Segura, I., De Bock, K., Hohensinner, P. J. and Carmeliet, P. (2009). Mechanisms of vessel branching: filopodia on endothelial tip cells lead the way. *Arterioscler. Thromb. Vasc. Biol.* **29**, 639-649.

Devenport, D. (2014). The cell biology of planar cell polarity. *J. Cell Biol.* **207**, 171-179.

Dormond, O., Foletti, A., Paroz, C. and Rüegg, C. (2001). NSAIDs inhibit alpha V beta 3 integrin-mediated and Cdc42/Rac-dependent endothelial-cell spreading, migration and angiogenesis. *Nat. Med.* **7**, 1041-1047.

Dubrac, A., Genet, G., Ola, R., Zhang, F., Pibouin-Fragner, L., Han, J., Zhang, J., Thomas, J.-L., Chedotal, A., Schwartz, M. A. et al. (2016). Targeting NCK-mediated endothelial cell front-rear polarity inhibits neovascularization. *Circulation* **133**, 409-421.

Ehling, M., Adams, S., Benedito, R. and Adams, R. H. (2013). Notch controls retinal blood vessel maturation and quiescence. *Development* **140**, 3051-3061.

Elias, B. C., Das, A., Parekh, D. V., Mernaugh, G., Adams, R., Yang, Z., Brakebusch, C., Pozzi, A., Marciano, D. K., Carroll, T. J. et al. (2015). Cdc42 regulates epithelial cell polarity and cytoskeletal function during kidney tubule development. *J. Cell. Sci.* **128**, 4293-4305.

Etienne-Manneville, S. (2004). Cdc42–the centre of polarity. *J. Cell. Sci.* **117**, 1291-1300.

Etienne-Manneville, S. and Hall, A. (2001). Integrin-mediated activation of Cdc42 controls cell polarity in migrating astrocytes through PKCzeta. *Cell* **106**, 489-498.

Fantin, A., Lampropoulou, A., Gestri, G., Raimondi, C., Senatore, V., Zachary, I. and Ruhrberg, C. (2015). NRP1 regulates CDC42 activation to promote filopodia formation in endothelial tip cells. *Cell Rep.* **11**, 1577-1590.

Franco, C. A., Jones, M. L., Bernabeu, M. O., Geudens, I., Mathivet, T., Rosa, A., Lopes, F. M., Lima, A. P., Ragab, A., Collins, R. T. et al. (2015). Dynamic endothelial cell rearrangements drive developmental vessel regression. *PLoS Biol.* **13**, e1002125.

Fruttiger, M. (2002). Development of the mouse retinal vasculature: angiogenesis versus vasculogenesis. *Invest. Ophthalmol. Vis. Sci.* **43**, 522-527.

Gebala, V., Collins, R., Geudens, I., Phng, L.-K. and Gerhardt, H. (2016). Blood flow drives lumen formation by inverse membrane blebbing during angiogenesis in vivo. *Nat. Cell Biol.* **18**, 443-450.

Gerhardt, H., Golding, M., Fruttiger, M., Ruhrberg, C., Lundkvist, A., Abramsson, A., Jeltsch, M., Mitchell, C., Alitalo, K., Shima, D. et al. (2003). VEGF guides angiogenic sprouting utilizing endothelial tip cell filopodia. *J. Cell Biol.* **161**, 1163-1177.

Geudens, I. and Gerhardt, H. (2011). Coordinating cell behaviour during blood vessel formation. *Development* **138**, 4569-4583.

Hall, A. (1998). Rho GTPases and the actin cytoskeleton. *Science* **279**, 509-514.

Heasman, S. J. and Ridley, A. J. (2008). Mammalian Rho GTPases: new insights into their functions from in vivo studies. *Nat. Rev. Mol. Cell Biol.* **9**, 690-701.

Hellström, M., Phng, L.-K., Hofmann, J. J., Wallgard, E., Coultas, L., Lindblom, P., Alva, J., Nilsson, A.-K., Karlsson, L., Gaiano, N. et al. (2007). Dll4 signalling through Notch1 regulates formation of tip cells during angiogenesis. *Nature* **445**, 776-780.

Horvat, R., Hovorka, A., Dekan, G., Poczewski, H. and Kerjaschki, D. (1986). Endothelial cell membranes contain podocalyxin–the major sialoprotein of visceral glomerular epithelial cells. *J. Cell Biol.* **102**, 484-491.

Jaffe, A. B. and Hall, A. (2005). Rho GTPases: biochemistry and biology. *Annu. Rev. Cell Dev. Biol.* **21**, 247-269.

Jin, Y., Liu, Y., Lin, Q., Li, J., Druso, J. E., Antonyak, M. A., Meininger, C. J., Zhang, S. L., Dostal, D. E., Guan, J.-L. et al. (2013). Deletion of Cdc42 enhances ADAM17-mediated vascular endothelial growth factor receptor 2 shedding and impairs vascular endothelial cell survival and vasculogenesis. *Mol. Cell. Biol.* **33**, 4181-4197.

Kaur, S., Castellone, M. D., Bedell, V. M., Konar, M., Gutkind, J. S. and Ramchandran, R. (2006). Robo4 signaling in endothelial cells implies attraction guidance mechanisms. *J. Biol. Chem.* **281**, 11347-11356.

Kesavan, G., Sand, F. W., Greiner, T. U., Johansson, J. K., Kobberup, S., Wu, X., Brakebusch, C. and Semb, H. (2009). Cdc42-mediated tubulogenesis controls cell specification. *Cell* **139**, 791-801.

Kim, J., Kim, Y. H., Kim, J., Park, D. Y., Bae, H., Lee, D.-H., Kim, K. H., Hong, S. P., Jang, S. P., Kubota, Y. et al. (2017). YAP/TAZ regulates sprouting angiogenesis and vascular barrier maturation. *J. Clin. Invest.* **127**, 3441-3461.

Kirjavainen, A., Laos, M., Anttonen, T. and Pirvola, U. (2015). The Rho GTPase Cdc42 regulates hair cell planar polarity and cellular patterning in the developing cochlea. *Biol. Open* **4**, 516-526.

Kouklis, P., Konstantoulaki, M. and Malik, A. B. (2003). VE-cadherin-induced Cdc42 signaling regulates formation of membrane protrusions in endothelial cells. *J. Biol. Chem.* **278**, 16230-16236.

Kroschewski, R., Hall, A. and Mellman, I. (1999). Cdc42 controls secretory and endocytic transport to the basolateral plasma membrane of MDCK cells. *Nat. Cell Biol.* **1**, 8-13.

Kupfer, A., Louvard, D. and Singer, S. J. (1982). Polarization of the Golgi apparatus and the microtubule-organizing center in cultured fibroblasts at the edge of an experimental wound. *Proc. Natl. Acad. Sci. USA* **79**, 2603-2607.

Kur, E., Kim, J., Tata, A., Comin, C. H., Harrington, K. I., Costa, L. D. F., Bentley, K. and Gu, C. (2016). Temporal modulation of collective cell behavior controls vascular network topology. *Elife* **5**, a001875.

Laurie, G. W., Leblond, C. P. and Martin, G. R. (1983). Light microscopic immunolocalization of type IV collagen, laminin, heparan sulfate proteoglycan, and fibronectin in the basement membranes of a variety of rat organs. *Am. J. Anat.* **167**, 71-82.

Lee, C. Y. and Bautch, V. L. (2011). Ups and downs of guided vessel sprouting: the role of polarity. *Physiology (Bethesda)* **26**, 326-333.

Lizama, C. O. and Zovein, A. C. (2013). Polarizing pathways: balancing endothelial polarity, permeability, and lumen formation. *Exp. Cell Res.* **319**, 1247-1254.

López-Colomé, A. M., Lee-Rivera, I., Benavides-Hidalgo, R. and López, E. (2017). Paxillin: a crossroad in pathological cell migration. *J. Hematol. Oncol.* **10**, 50.

Madisen, L., Zwingman, T. A., Sunkin, S. M., Oh, S. W., Zariwala, H. A., Gu, H., Ng, L. L., Palmiter, R. D., Hawrylycz, M. J., Jones, A. R. et al. (2010). A robust and high-throughput Cre reporting and characterization system for the whole mouse brain. *Nat. Neurosci.* **13**, 133-140.

Martín-Belmonte, F., Gassama, A., Datta, A., Yu, W., Rescher, U., Gerke, V. and Mostov, K. (2007). PTEN-mediated apical segregation of phosphoinositides controls epithelial morphogenesis through Cdc42. *Cell* **128**, 383-397.

Martín-Belmonte, F., Yu, W., Rodríguez-Fraticelli, A. E., Ewald, A. J., Ewald, A., Werb, Z., Alonso, M. A. and Mostov, K. (2008). Cell-polarity dynamics controls the mechanism of lumen formation in epithelial morphogenesis. *Curr. Biol.* **18**, 507-513.

Meder, D., Shevchenko, A., Simons, K. and Füllekrug, J. (2005). Gp135/podocalyxin and NHERF-2 participate in the formation of a preapical domain during polarization of MDCK cells. *J. Cell Biol.* **168**, 303-313.

Melendez, J., Grogg, M. and Zheng, Y. (2011). Signaling role of Cdc42 in regulating mammalian physiology. *J. Biol. Chem.* **286**, 2375-2381.

Niaudet, C., Hofmann, J. J., Mäe, M. A., Jung, B., Gaengel, K., Vanlandewijck, M., Ekvärn, E., Salvado, M. D., Mehlem, A., Al Sayegh, S. et al. (2015). Gpr116 receptor regulates distinctive functions in pneumocytes and vascular endothelium. *PLoS ONE* **10**, e0137949.

Nobes, C. D. and Hall, A. (1995). Rho, rac, and cdc42 GTPases regulate the assembly of multimolecular focal complexes associated with actin stress fibers, lamellipodia, and filopodia. *Cell* **81**, 53-62.

Pitulescu, M. E., Schmidt, I., Benedito, R. and Adams, R. H. (2010). Inducible gene targeting in the neonatal vasculature and analysis of retinal angiogenesis in mice. *Nat. Protoc.* **5**, 1518-1534.

Sakabe, M., Fan, J., Odaka, Y., Liu, N., Hassan, A., Duan, X., Stump, P., Byerly, L., Donaldson, M., Hao, J. et al. (2017). YAP/TAZ-CDC42 signaling regulates vascular tip cell migration. *Proc. Natl. Acad. Sci. USA* **114**, 10918-10923.

Srinivas, S., Watanabe, T., Lin, C.-S., William, C. M., Tanabe, Y., Jessell, T. M. and Costantini, F. (2001). Cre reporter strains produced by targeted insertion of EYFP and ECFP into the ROSA26 locus. *BMC Dev. Biol.* **1**, 4.

Stahl, A., Connor, K. M., Sapieha, P., Chen, J., Dennison, R. J., Krah, N. M., Seaward, M. R., Willett, K. L., Aderman, C. M., Guerin, K. I. et al. (2010). The mouse retina as an angiogenesis model. *Invest. Ophthalmol. Vis. Sci.* **51**, 2813-2826.

Strilić, B., Kučera, T., Eglinger, J., Hughes, M. R., McNagny, K. M., Tsukita, S., Dejana, E., Ferrara, N. and Lammert, E. (2009). The molecular basis of vascular lumen formation in the developing mouse aorta. *Dev. Cell* **17**, 505-515.

Strilić, B., Eglinger, J., Krieg, M., Zeeb, M., Axnick, J., Babál, P., Müller, D. J. and Lammert, E. (2010). Electrostatic cell-surface repulsion initiates lumen formation in developing blood vessels. *Curr. Biol.* **20**, 2003-2009.

Tkachenko, E., Lutgens, E., Stan, R.-V. and Simons, M. (2004). Fibroblast growth factor 2 endocytosis in endothelial cells proceed via syndecan-4-dependent

activation of Rac1 and a Cdc42-dependent macropinocytic pathway. *J. Cell. Sci.* **117**, 3189-3199.

Ubezio, B., Blanco, R. A., Geudens, I., Stanchi, F., Mathivet, T., Jones, M. L., Ragab, A., Bentley, K. and Gerhardt, H. (2016). Synchronization of endothelial Dll4-Notch dynamics switch blood vessels from branching to expansion. *Elife* **5**, 186.

Vitorino, P. and Meyer, T. (2008). Modular control of endothelial sheet migration. *Genes Dev.* **22**, 3268-3281.

Wakayama, Y., Fukuhara, S., Ando, K., Matsuda, M. and Mochizuki, N. (2015). Cdc42 mediates Bmp-induced sprouting angiogenesis through Fmnl3-driven assembly of endothelial filopodia in zebrafish. *Dev. Cell* **32**, 109-122.

Wan, H., Liu, C., Wert, S. E., Xu, W., Liao, Y., Zheng, Y. and Whitsett, J. A. (2013). CDC42 is required for structural patterning of the lung during development. *Dev. Biol.* **374**, 46-57.

Wassef, M., Blei, F., Adams, D., Alomari, A., Baselga, E., Berenstein, A., Burrows, P., Frieden, I. J., Garzon, M. C., Lopez-Gutierrez, J.-C. et al. (2015). Vascular anomalies classification: recommendations from the international society for the study of vascular anomalies. *Pediatrics* **136**, e203-e214.

Wójciak-Stothard, B., Entwistle, A., Garg, R. and Ridley, A. J. (1998). Regulation of TNF-alpha-induced reorganization of the actin cytoskeleton and cell-cell junctions by Rho, Rac, and Cdc42 in human endothelial cells. *J. Cell. Physiol.* **176**, 150-165.

Wu, X., Quondamatteo, F., Lefever, T., Czuchra, A., Meyer, H., Chrostek, A., Paus, R., Langbein, L. and Brakebusch, C. (2006). Cdc42 controls progenitor cell differentiation and beta-catenin turnover in skin. *Genes Dev.* **20**, 571-585.

Xu, C., Hasan, S. S., Schmidt, I., Rocha, S. F., Pitulescu, M. E., Bussmann, J., Meyen, D., Raz, E., Adams, R. H. and Siekmann, A. F. (2014). Arteries are formed by vein-derived endothelial tip cells. *Nat. Commun.* **5**, 5758.

Figure S1

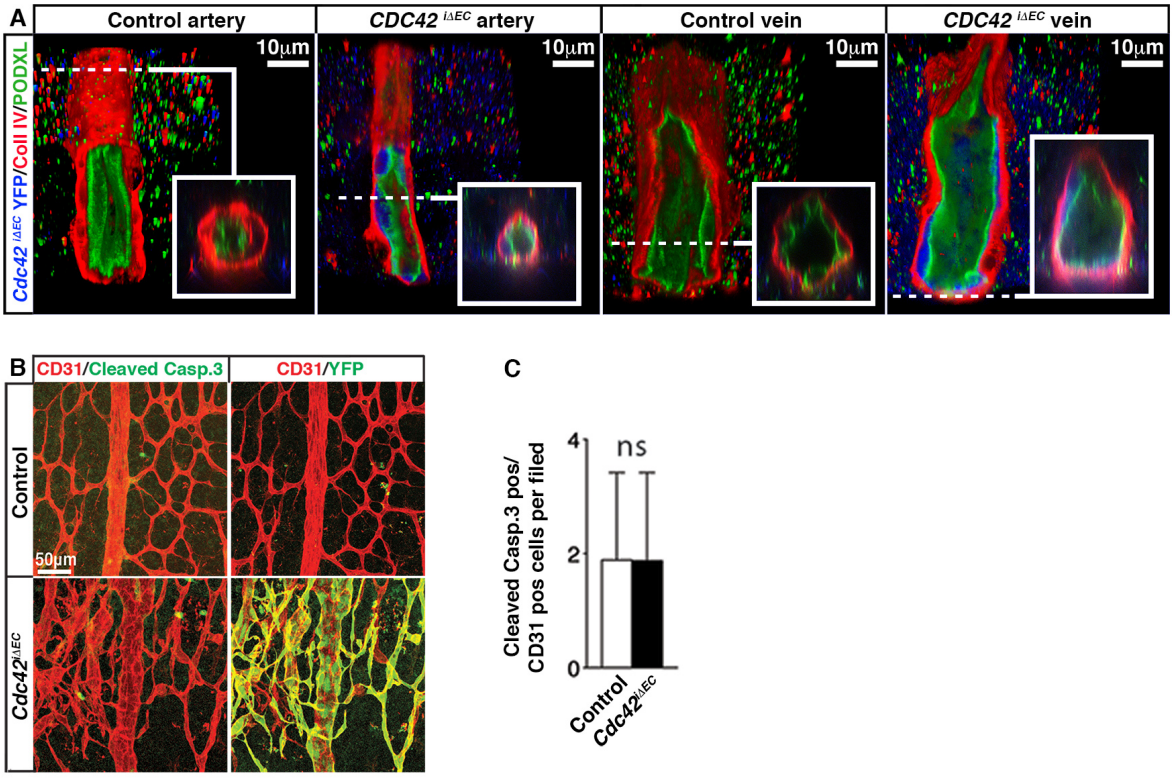

Figure S1: Loss of Cdc42 does not compromise endothelial apical-basal polarity nor EC survival during postnatal retinal development (A) 3-D reconstructions and optical sections of arteries and veins from P7 control and *Cdc42*$^{i\Delta EC}$ retinas. Dashed lines indicate the location of the cross-sectional view shown in the boxed areas. Podocalyxin (PODXL) (green) marks the apical (luminal) surface of blood vessels, while Coll IV stains the basal (abluminal) surface. Note that apical-basal polarization of blood vessels in *Cdc42*$^{i\Delta EC}$retinas appears normal and that YFP+ (*Cdc42*KO-EC) cells (blue) are properly located between the apical and basal domains. **(B)** Analysis of EC apoptosis in P7 control and *Cdc42*$^{i\Delta EC}$ retinas stained for ECs (CD31) and apoptosis (cleaved caspase-3). **(C)** Quantification of apoptotic ECs in the retina vasculature (control n=18 fields; *Cdc42*$^{i\Delta EC}$ n=18 fields from 2 animals per group from 2 independent litters). Graph shows mean ± s.d (Unpaired two-tailed t-test, ns – non significant).

Figure S2

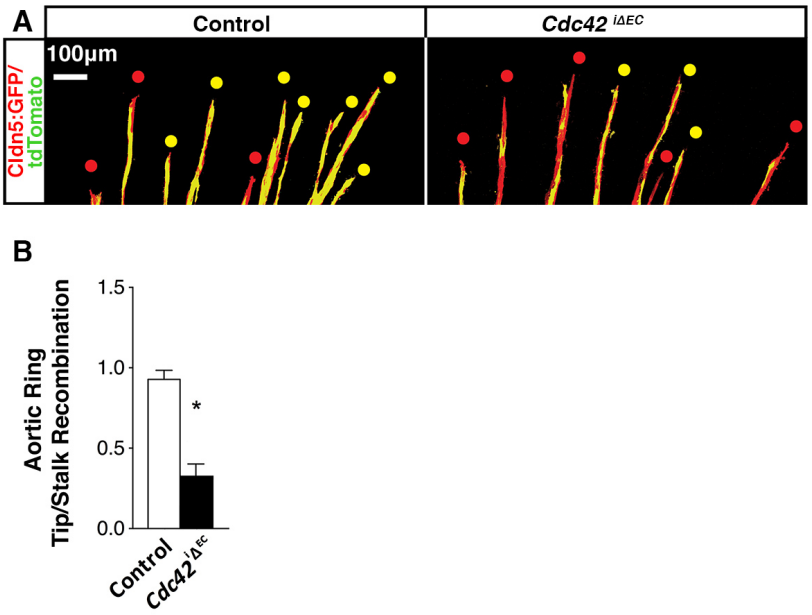

Figure S2: Cdc42 is required for endothelial tip selection in aortic rings cultures

(A) Confocal images of aortic ring sprouts from control and *Cdc42*$^{i\Delta EC}$ mice. Cldn5:GFP expression labels all ECs (red); recombined ECs labeled by tdTomato (green). Based on tdTomato expression we calculated the recombination rate to be 90±0.04%. Red dots denote non-recombined tip cells and yellow dots recombined tip cells. **(B)** Quantification of tip/stalk cell recombination in aortic rings from control (n=8) and *Cdc42*$^{i\Delta EC}$ (n=12) animals (at least 225 sprouts were analyzed per group). Graph shows mean ± s.d (Unpaired two-tailed t-test; * $p \leq 0.01$).

Figure S3

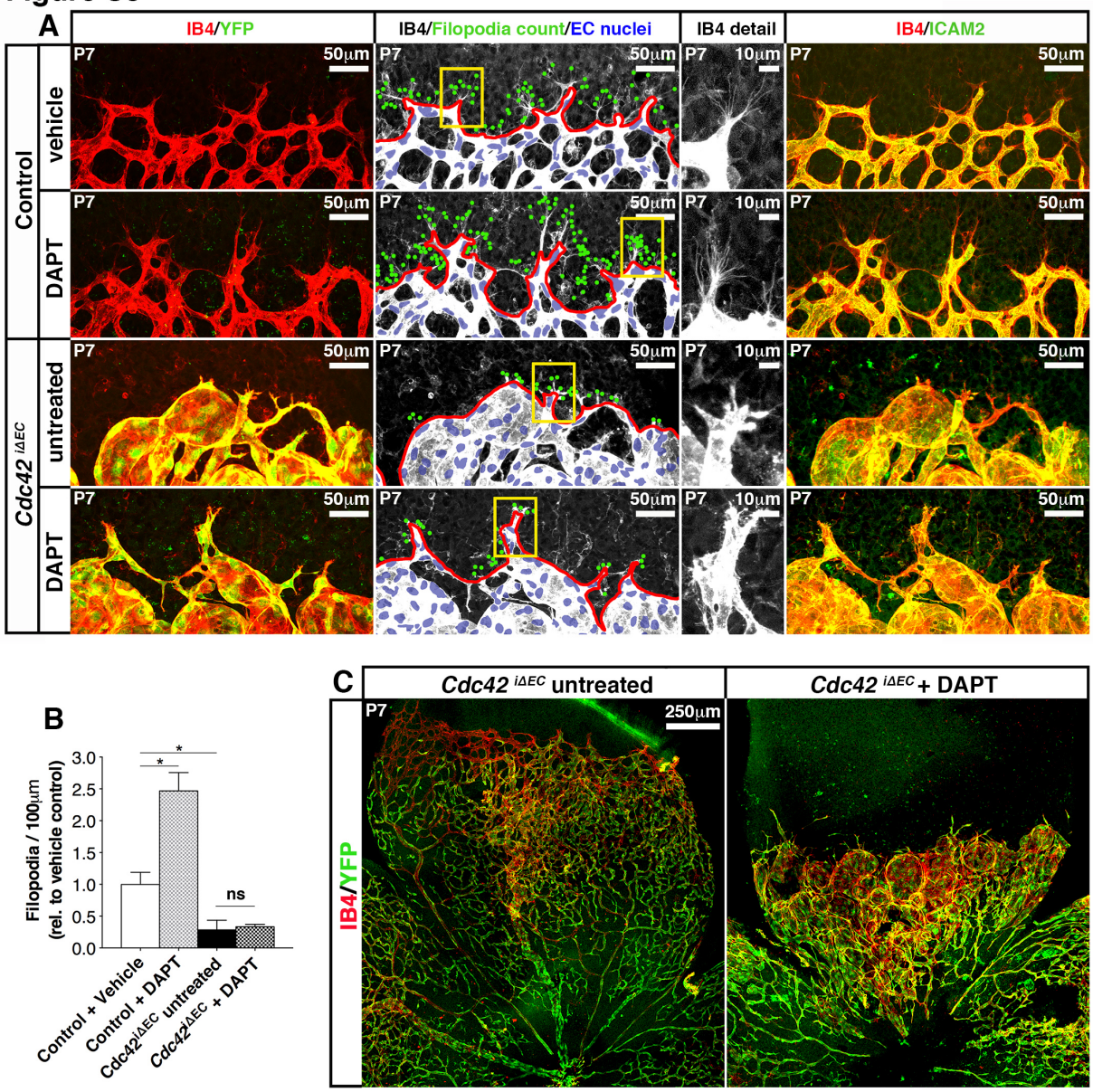

Figure S3: Pharmacological inhibition of Notch signaling fails to induce filopodia formation in *Cdc42*$^{i\Delta EC}$ retinas but aggravates vascular malformations

(A) Confocal images of P7 control and *Cdc42*$^{i\Delta EC}$ retinas (untreated, vehicle treated or treated with the γ-secretase inhibitor DAPT for 12hours). EC are labeled with IB4, recombinant cells by YFP and vascular lumens by ICAM2. Single filopodia are indicated by green dots and the position of EC nuclei are indicated based on ERG staining. Red lines delineate the vascular front length. Yellow boxes indicate tip cells shown in higher resolution to the right. Note that DAPT induces filopodia formation (green dots) in the control group but not in *Cdc42*$^{i\Delta EC}$ retinas. **(B)** Quantification of filopodia per 100µm vascular front; Control+Vehicle (n=3); Control+DAPT (n=4); *Cdc42*$^{i\Delta EC}$ untreated (n=9); *Cdc42*$^{i\Delta EC}$+DAPT (n=3); values indicate mean±s.d. Between 65 and 120 tip cells were analyzed per group. Graph shows mean ±

s.d (Unpaired two-tailed t-test, ns – non significant; * p≤0.05). **(C)** Overview confocal images showing vascular malformation in DAPT treated and untreated P7 *Cdc42*^{iAEC} retinas. Note how DAPT treatment aggravates the vascular malformations.

Figure S4

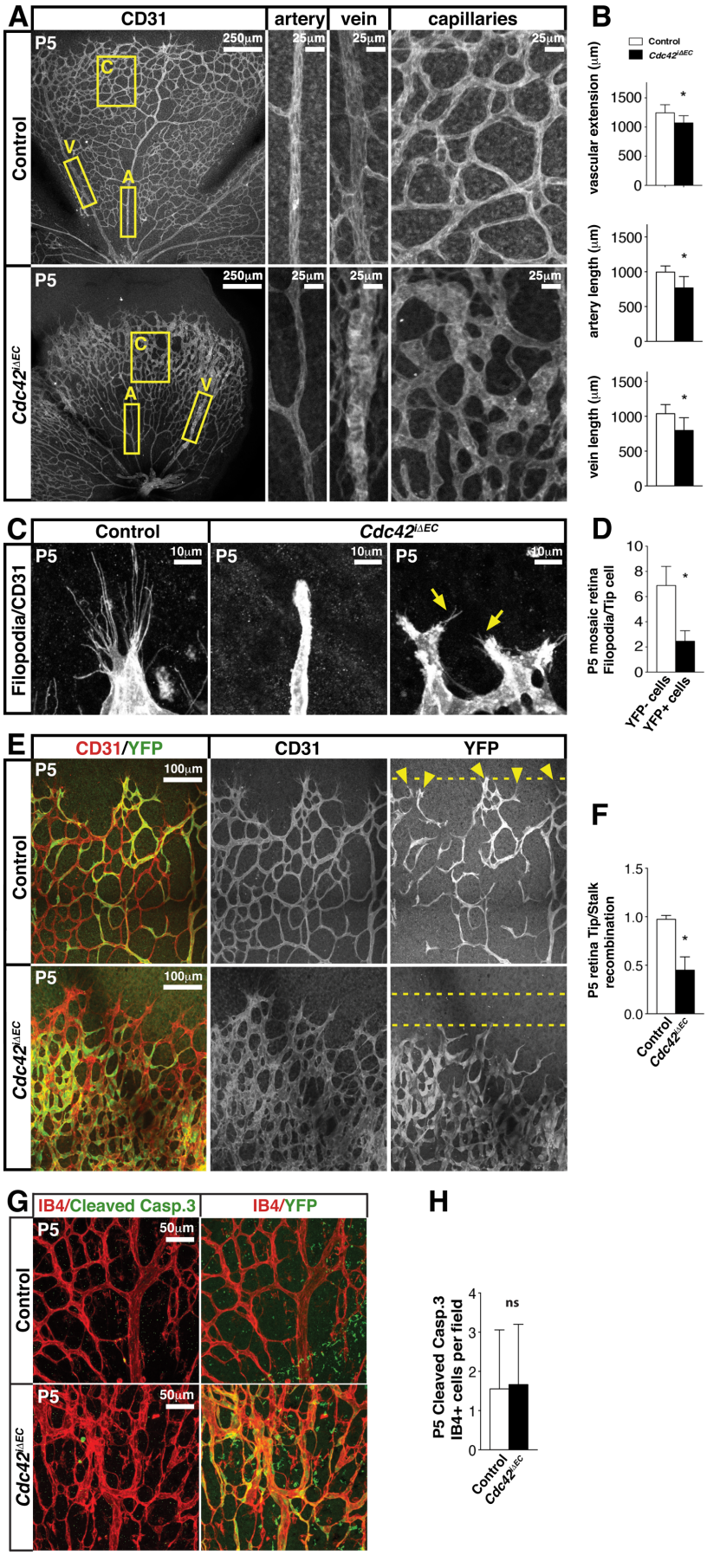

Figure S4: Vascular phenotypes in P5 *Cdc42*$^{i\Delta EC}$ retinas

(A) P5 retinal whole-mounts stained with CD31 to visualized blood vessels. Note the reduced vascular expansion towards the retinal periphery and vascular malformations in veins (V) and capillaries (C), but not in arteries (A) of *Cdc42*$^{i\Delta EC}$ retinas. Right panels: high-magnification images of boxed areas reveal tortuous dilations in vein and capillaries, and protuberant endothelial structures in *Cdc42*$^{i\Delta EC}$ retinas. **(B)** Quantification of vascular extension and of arterial and venous length in P5 control (n=7) and *Cdc42*$^{i\Delta EC}$ retinas (n=5); *p<0.05. **(C)** ECs in the tip cell position from control and highly recombined (>80%) *Cdc42*$^{i\Delta EC}$ P5 retinas labeled with CD31. Note that *Cdc42*KO-EC at tip cell positions are morphologically abnormal and had a significant decrease in number of filopodia (indicated by yellow arrows). **(D)** Quantification of filopodia number per tip cell in highly recombined P5 *Cdc42*$^{i\Delta EC}$ (n=3) retinas; more than 125 tip cells were analyzed; *p<0.05. (E) Images of sprouting front areas showing the distribution of recombinant cells (YFP+) in P5 control and

Cdc42$^{i\Delta EC}$ retinas stained for ECs (CD31) and YFP. Yellow arrowheads indicate recombinant endothelial tip cells (YFP+) and yellow dashed lines mark vascular areas where no recombinant cells are found. **(F)** Quantification of TR/SR ratios in P5 control (n=5) and *Cdc42*$^{i\Delta EC}$ (n=5) retinas showing a disadvantage of *Cdc42*KO-EC to be in the tip cell position as shown in P7 retinas;
*p<0.05. **(G)** Analysis of EC apoptosis in P5 control and *Cdc42*$^{i\Delta EC}$ retinas stained for ECs (IB4) and apoptosis (cleaved caspase-3). **(H)** Quantification of apoptotic ECs in the retina vasculature (control n=2 and *Cdc42*$^{i\Delta EC}$ n=3 from 2 independent litters). Graphs show mean ± s.d (Unpaired two-tailed t-test, ns – non significant; * p≤0.05).

Figure S5

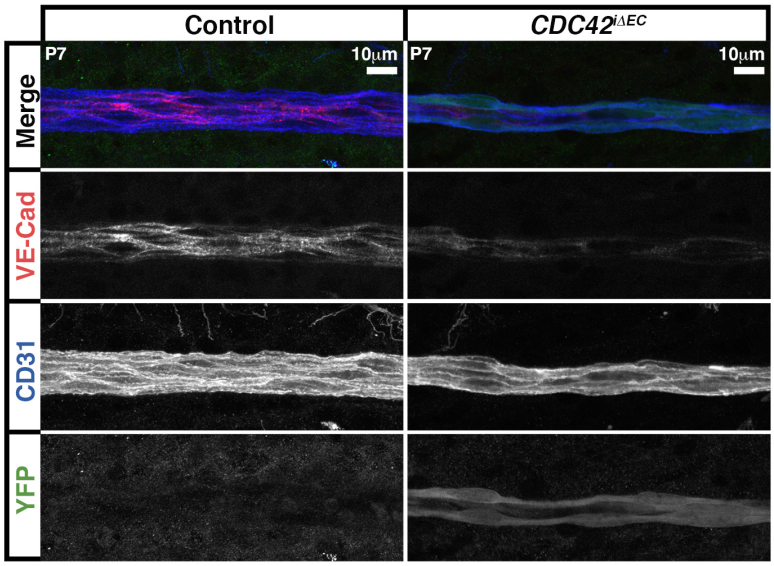

Figure S5: Effects on EC junctions in *Cdc42*$^{\Delta EC}$ arteries.

Confocal images of highly recombined arteries from control and *Cdc42*$^{\Delta EC}$ retinas at P7, stained for YFP (green, to visualize recombination efficiency), VE-Cadherin (red) and CD31 (blue). Note that Cdc42 deficiency leads to disturbed VE-Cadherin localization at arterial EC junctions *in vivo* but that overall arterial morphology is not severely affected.

Figure S6

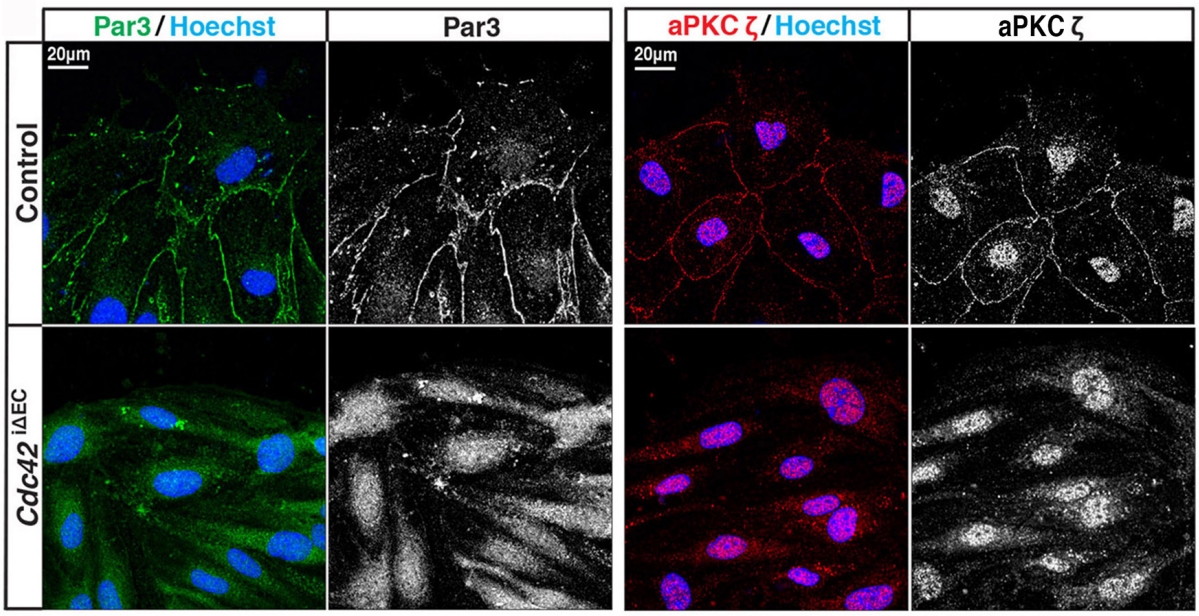

Figure S6: Cellular localization of Par complex proteins

Confocal images of primary brain ECs isolated from P7 control and *Cdc42*^{iΔEC} animals stained for Par3, atypical Protein Kinase C (aPKCζ) and Hoechst. Note that the membrane associated localization of Par3, and aPKCζ is lost in the absence of Cdc42.

Figure S7

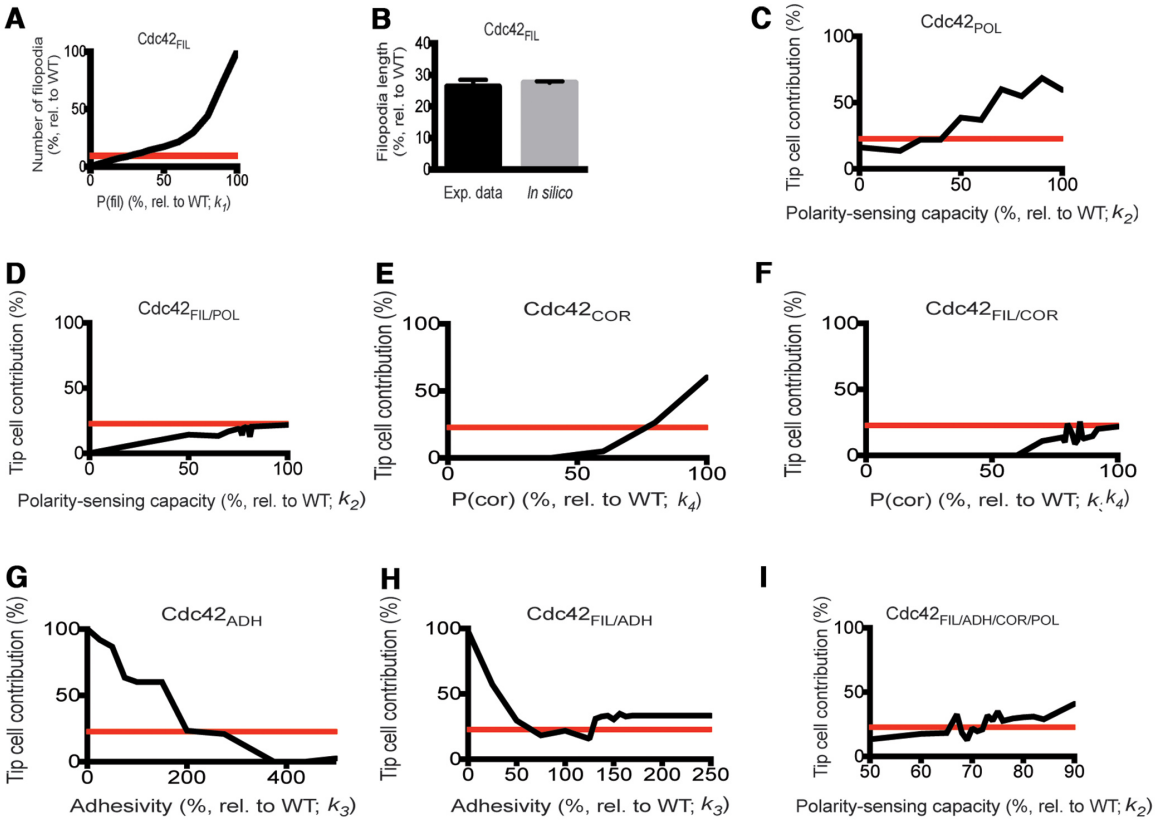

Figure S7: Computational modeling of the different Cdc42 driven cellular processes impacting on sprouting

(A) Sensitivity analysis of $Cdc42_{FIL}$ depicting dependence of filopodia number on the probability to extend filopodia in MSM-CPM (P(fil)). The red line indicates the experimentally observed reduction in filopodia number. **(B)** Filopodia length quantification (% relative to WT) in our experimental data (Exp. data) and *in silico* using the $Cdc42_{FIL}$ model. **(C-I)** Sensitivity analyses showing how the *Cdc42*KO cell contribution to the tip in simulated 6:4 *Cdc42*KO:WT sprouts changes when **(C)** polarity-sensing capacity ($Cdc42_{POL}$), **(E)** the probability of extending junctional cortex protrusions ($Cdc42_{COR}$) and **(G)** intercellular adhesion ($Cdc42_{ADH}$) are modified independently or in combination **(D, F, H, I)**. The red line indicates the experimentally observed *Cdc42*KO cell contribution to the tip for 6:4 *Cdc42*KO:WT sprouts.

Figure S8

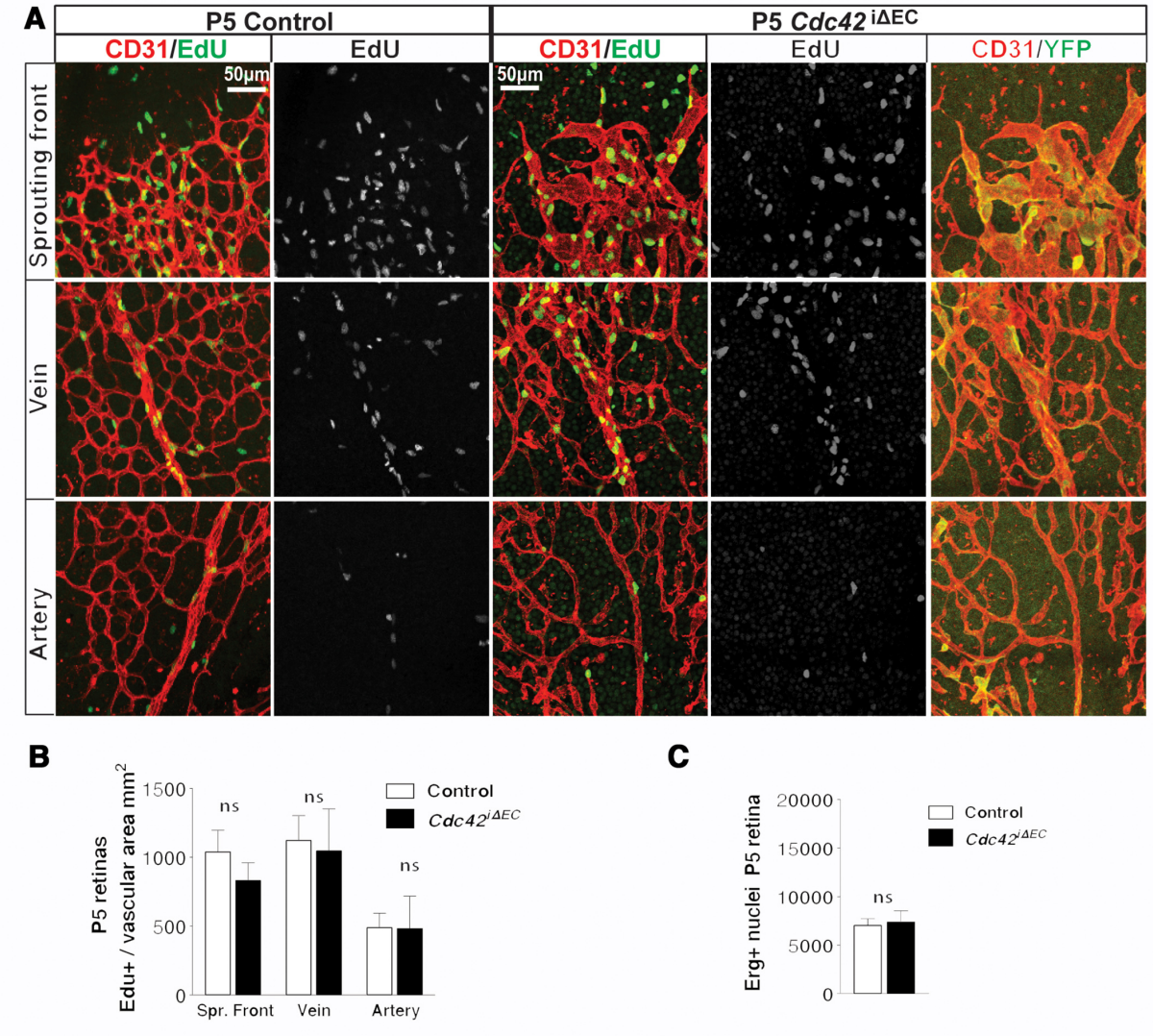

Figure S8: EC proliferation is not altered in P5 retinas

Analysis of EC proliferation in the sprouting front, veins and arteries of control and *Cdc42*$^{i\Delta EC}$ retinas. **(A)** Confocal images from P5 control and *Cdc42*$^{i\Delta EC}$ retina stained for ECs (CD31), proliferating cells (EdU), and recombination efficiency (YFP). **(B)** Quantification of EC proliferation in P5 retinas displayed as proliferating (EdU +) cells per vascular area in control (n=4) and *Cdc42*$^{i\Delta EC}$ (n=5) **(C)** Total number of ECs (ERG +) in control (n=3) and *Cdc42*$^{i\Delta EC}$ (n=4) retinas at P5. Graph shows mean ± s.d (Unpaired two-tailed t-test, ns – non significant)

Table S1

A

		1st row		2nd row		3rd row	
Wound assay	**N° wounds analysed**	**N° cells analysed**	**% Polarized ECs**	**N° cells analysed**	**% Polarized ECs**	**N° cells analysed**	**% Polarized ECs**
5h Control	8	205	**77.7**	61	**74.7**	65	**59.9**
5h Cdc42 $^{i\Delta EC}$	11	297	**38.7**	123	**36.2**	119	**35.3**
24h Control	10	554	**80.0**	145	**78.7**	151	**76.3**
24h Cdc42 $^{i\Delta EC}$	8	526	**38.3**	78	**33.9**	74	**34.9**

B

	Artery		Vein		Capillaries at sprouting front		
P7 Retina	N° Cells analysed	% Polarized ECs	N° Cells analysed	% Polarized ECs	N° Cells analysed	% Polarized ECs at -180°C	% Polarized ECs at 0°
Control	120	**98.3**	219	**87.2**	361	**39.85**	**39.88**
Cdc42 $^{i\Delta EC}$	125	**97.6**	389	**46.0**	332	**18.74**	**35.74**

Table S1: Quantitative analysis of EC axial polarity

Detailed quantitative analysis of EC axial polarity in **(A)** scratch wound assay performed with primary brain ECs isolated from P7 control and *Cdc42*$^{i\Delta EC}$ mice, 5h (Control n=8; *Cdc42*$^{i\Delta EC}$ n=11) and 24h (Control n=10; *Cdc42*$^{i\Delta EC}$ n=8) post scratch in the 1st, 2nd and 3th cell row and **(B)** arteries (n=3), veins (n=3) and capillaries at the sprouting front (n=6) from P7 control and *Cdc42*$^{i\Delta EC}$ retinas. See material and methods section and Fig. 5 and 6 for more information about quantification method used in this analysis.

Movies

Cdc42 is dispensable for endothelial lumen formation in the postnatal retina

Movie 1

Movie 2

Movie 3

Movie 4

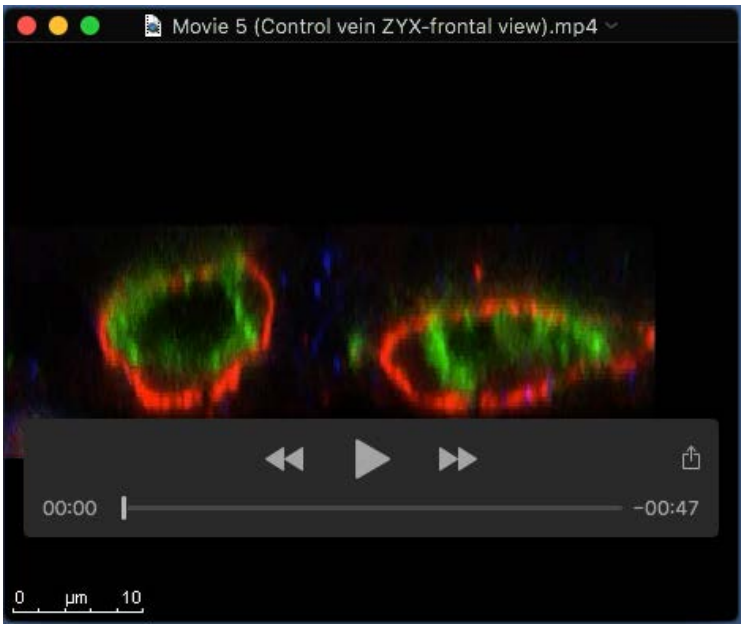

Movie 5

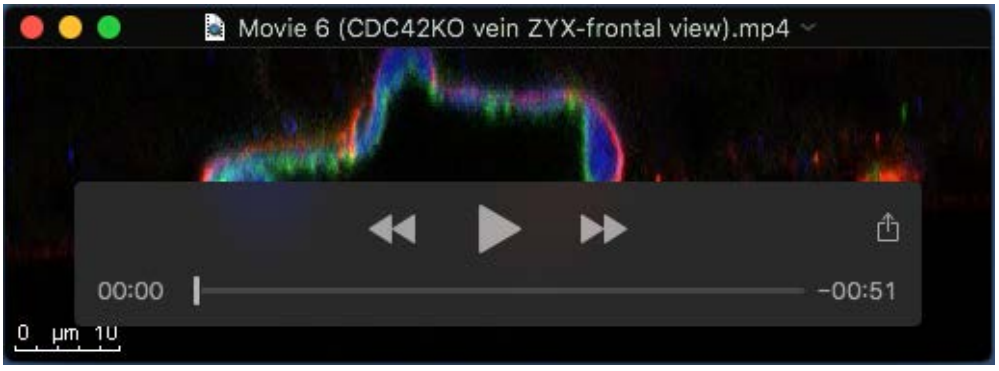

Movie 6

Movie 7

Movie 8

Movies 1-8: Animation of continuous optical ZYX (frontal view movies 1,2,5,6) and ZXY (lateral view movies 3,4,7,8) sections of arteries and veins from P7 control and *Cdc42*$^{\Delta EC}$ retinas. The abluminal (basal) surface of the endothelium is stained for Coll IV (red) while the luminal (apical) surface of the endothelium is identified by the ICAM2 staining (green). YFP expression indicates *Cdc42*KO-EC (pseudocolored in blue). Note that apical basal polarization and lumen formation in *Cdc42*$^{\Delta EC}$ arteries and veins appears normal but that veins are dilated.

1: ZYX (frontal) view of a control artery

2: ZYX (frontal) view of a *Cdc42*$^{\Delta EC}$ artery

3: ZXY (lateral) view of the control artery in S1

4: ZXY (lateral) view of the *Cdc42*$^{\Delta EC}$ artery in S2

5: ZYX (frontal) view of a control vein

6: ZYX (frontal) view of a *Cdc42*$^{\Delta EC}$ vein

7: ZXY (lateral) view of the control vein in S5

8: ZXY (lateral) view of the *Cdc42*$^{\Delta EC}$ vein in S6

Movie 9

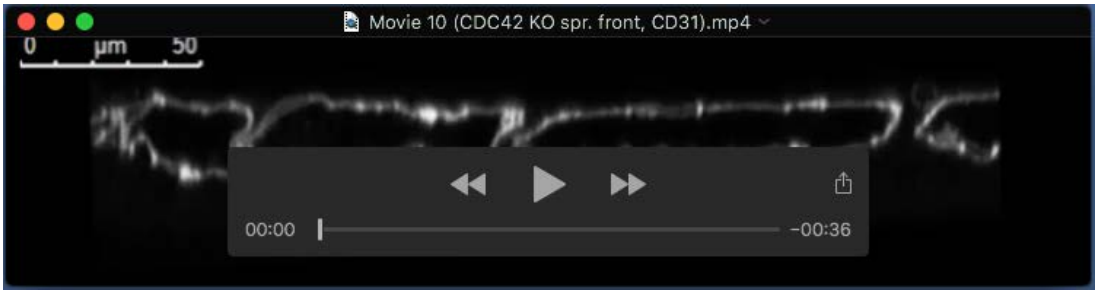

Movie 10

Movies 9, 10: Animation of continuous optical ZYX sections of blood vessels at the sprouting front (allowing a view into the vessel lumen) of P7 retinas. The image sequence is oriented proximal to distal with the first frame being located at more mature vessels of the sprouting front and the last frames ending with endothelial tip cells. Blood vessels stained with CD31 antibody (white). Vascular lumen of the sprouting front in control (**Movie 9**) and *Cdc42*$^{\Delta EC}$ retinas (**Movie 10**)

Movie 11: Capillary-venous malformations in *Cdc42*$^{i\Delta EC}$ retinas

3-D reconstruction and subsequent animation of confocal sections from a P7 *Cdc42*$^{i\Delta EC}$ retina stained with CD31. The confocal sections were acquired in the capillary network proximal to the sprouting front. Note the formation of large interconnected lumens in the cavernous like structures.

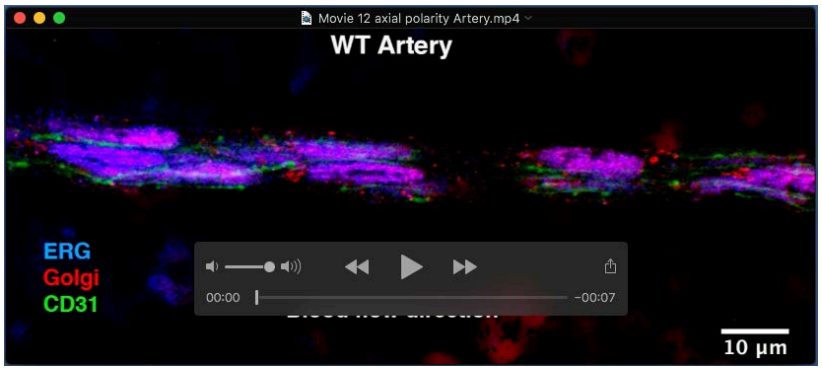

Movie 12: Evaluation of EC axial polarization *in-vivo*

Illustration of how EC polarization was quantified *in vivo* using individual sections of a z-stack. This example shows a representative control artery at P7. ERG (blue), CD31 (Green), and Golph4 (Red) stainings were combined to evaluate Golgi polarization. Confocal images were acquired at high magnification and the sequential z-slices from different channels were merged into a single hyperstack using FIJI software. Arterial ECs are highly polarized and orient their Golgi in front of the nucleus facing the predicted direction of blood flow (arrows).

Movie 13

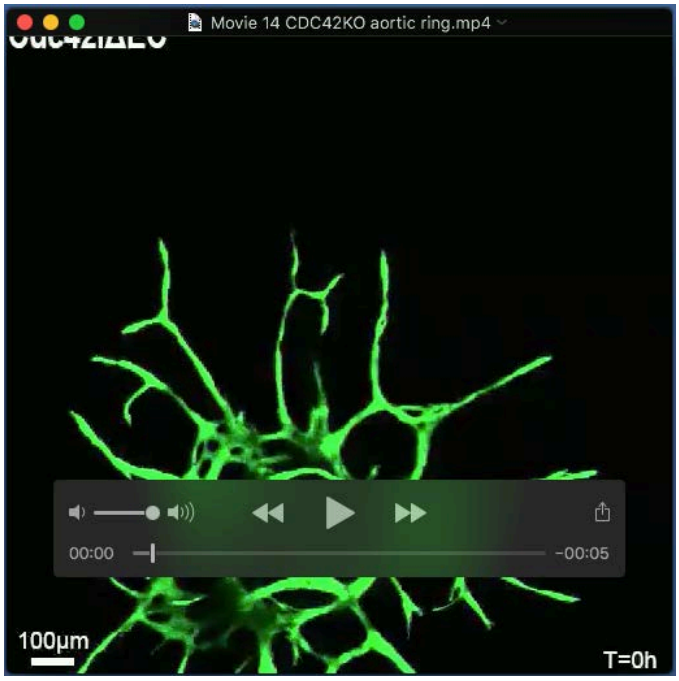

Movie 14

Movies 13,14: Time-lapse movies (47h) of Cldn5:GFP positive aortic rings from control **(Movie 13)** and *Cdc42*$^{\Delta EC}$ mice **(Movie 14)**.

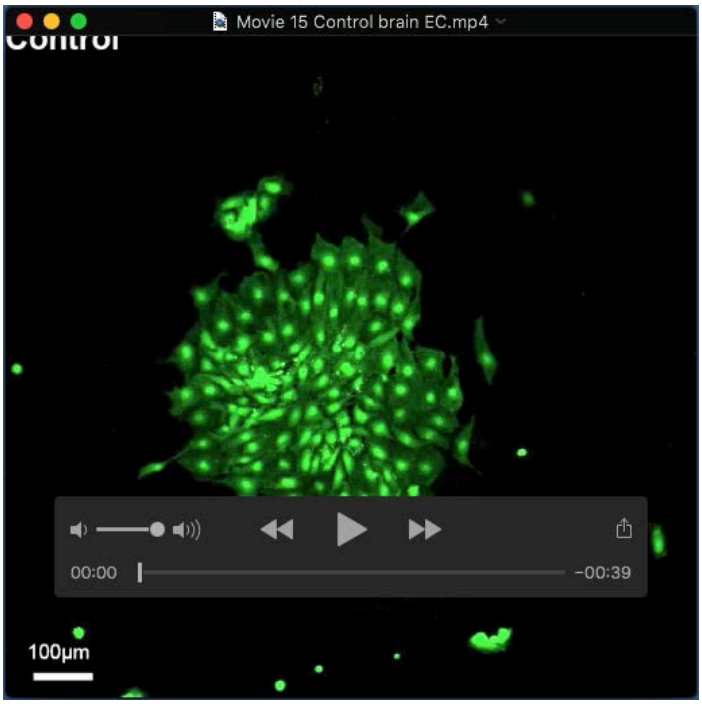

Movie 15

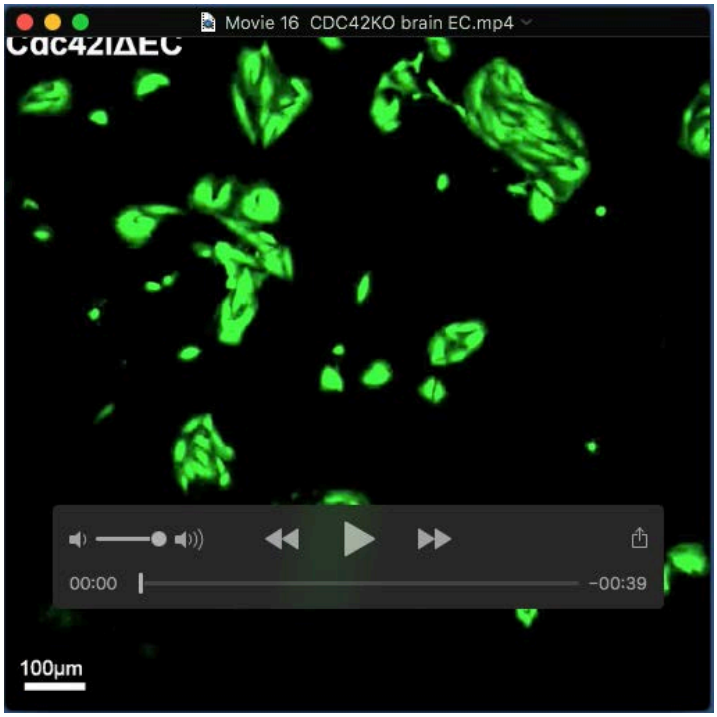

Movie 16

Movies 15, 16: Time-lapse movies (97h) of Cldn5:GFP positive primary brain EC clusters isolated from P7 control (**Movie 15**) and *Cdc42*^{iEC}(**Movie 16**) animals.

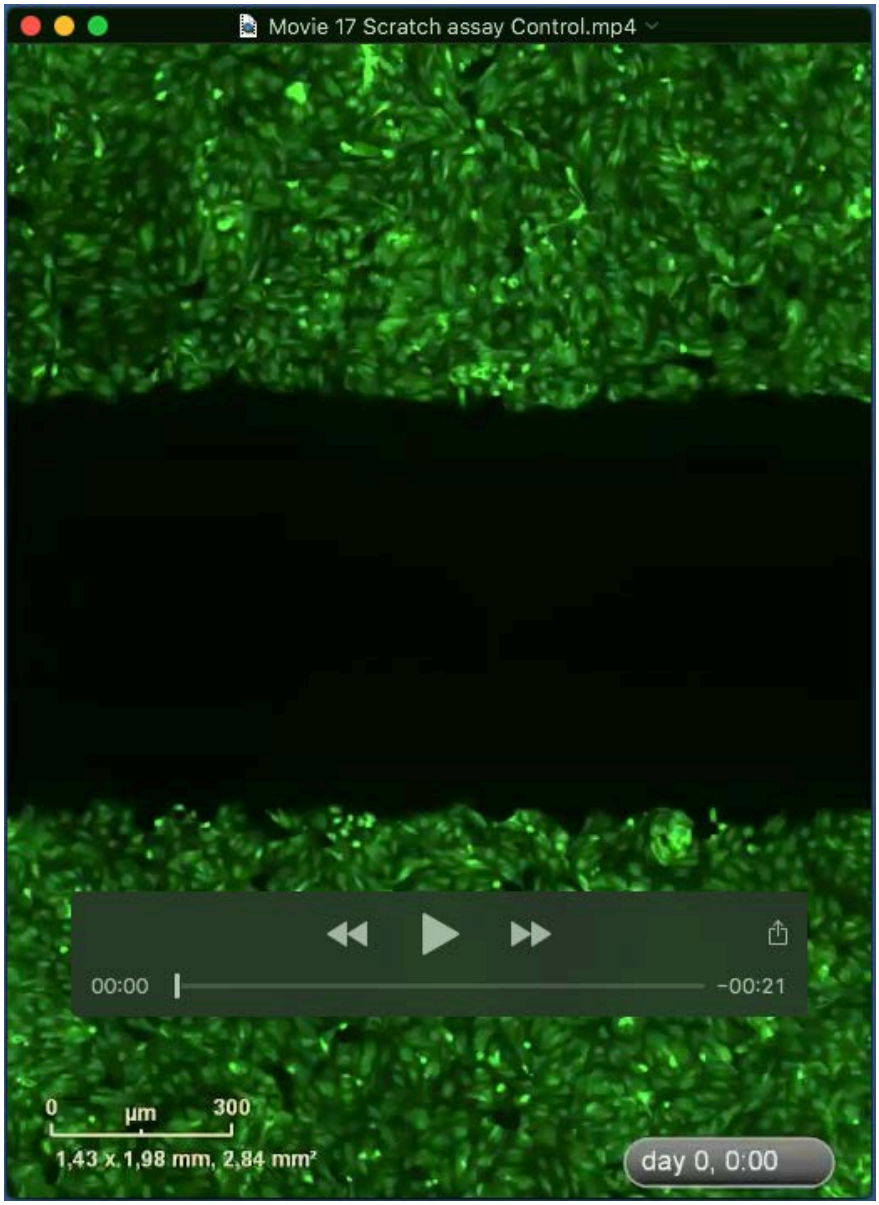

Movie 17

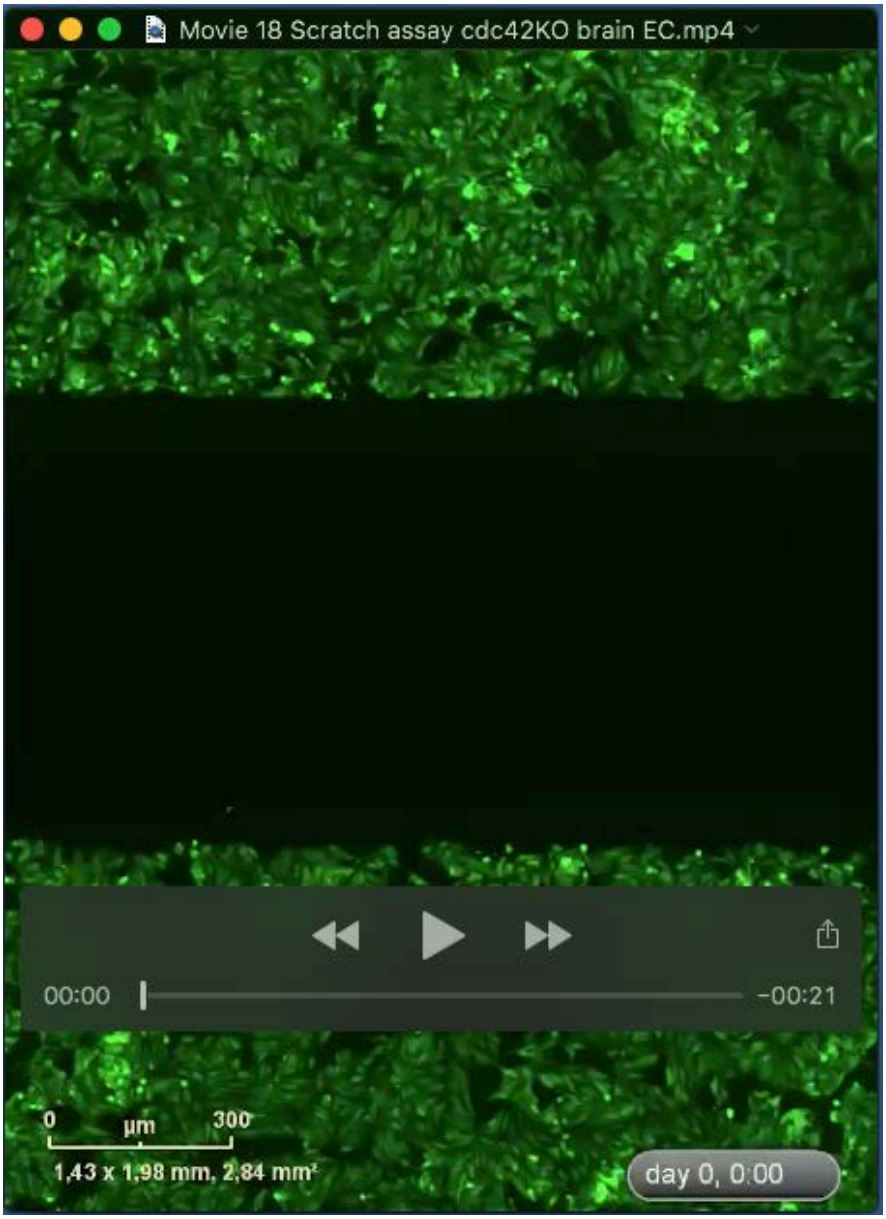

Movie 18

Movies 17, 18: Time-lapse movies (72h) of scratch assay from primary brain ECs (Cldn5:GFP positive) isolated from P7 control (**Movie 17**) and *Cdc42*$^{\Delta EC}$ (**Movie 18**) animals.

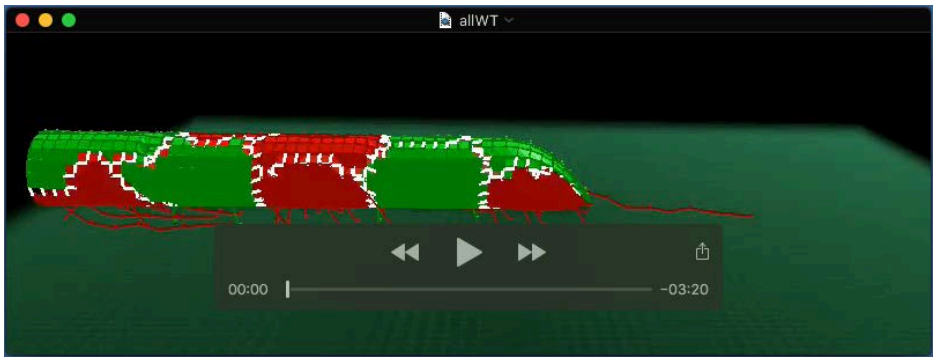

Movie 19: WT:WT sprout

Simulation movie showing a 1:1 WT:WT sprout in which both the green and red cells depict WT cells. The green and red cells are equally competent to occupy the tip position. The green layer underneath the vessel shows the VEGF gradient, which linearly increases towards the tip.

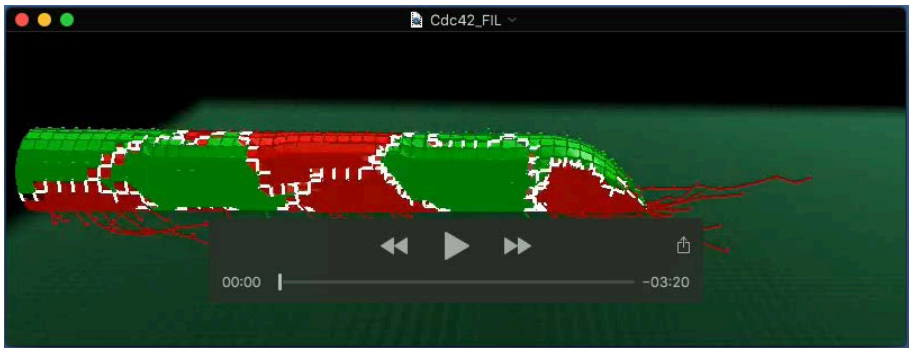

Movie 20: $Cdc42_{FIL}$:WT sprout

Simulation movie showing a 1:1 $Cdc42_{FIL}$:WT sprout in which the green and red cells respectively depict $Cdc42_{FIL}$ and WT cells. The green $Cdc42_{FIL}$ mutant cells extend less filopodia and are less competent to occupy the tip position than the red WT cells. The $Cdc42_{FIL}$ and WT cells segregate vertically, with the $Cdc42_{FIL}$ and WT cells respectively at the top and bottom of the vessel sprout, and this in a persistent way (compare with $Cdc42_{POL}$:WT sprout in Movie 22). They additionally segregate horizontally, with the $Cdc42_{FIL}$ cells at the rear of the sprout, albeit in a rather transient way (compare with $Cdc42_{POL}$:WT sprout in Movie 22). The green layer underneath the vessel shows the VEGF gradient, which linearly increases towards the tip.

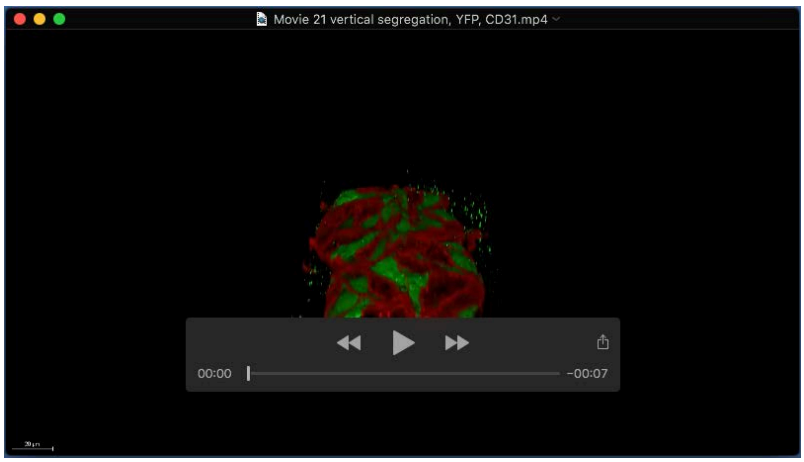

Movie 21: Vertical segregation of *Cdc42*KO-EC *in vivo*

Endothelial cells lacking Cdc42 preferentially occupy the upper side (facing the vitreous) of growing blood vessels and are underrepresented on the bottom side of vessels (facing the astrocytes). 3-D animation of a XYZ Confocal stack, showing a partially recombined vein in a P7 *Cdc42*^{iEC} retina. *Cdc42*KO cells are indicated by YFP expression (green), ECs are visualized by CD31 staining (red).

Movie 22: Cdc42$_{POL}$:WT sprout

Simulation movie showing a 1:1 Cdc42$_{POL}$:WT sprout in which the green and red cells respectively depict Cdc42$_{POL}$ and WT cells. The green Cdc42$_{POL}$ cells are less polarized and are less competent to occupy the tip position than the red WT cells. The Cdc42$_{POL}$ and WT cells segregate vertically, with the Cdc42$_{POL}$ and WT cells respectively at the top and bottom of the vessel sprout, albeit only transiently (compare with Cdc42$_{FIL}$:WT sprout in Movie 21). In contrast, the horizontal segregation of the Cdc42$_{POL}$ and WT cells, with the Cdc42$_{POL}$ cells at the rear of the sprout, occurs in a more persistent way (compare with Cdc42$_{FIL}$:WT sprout in Movie 21). The green layer underneath the vessel shows the VEGF gradient, which linearly increases towards the tip.

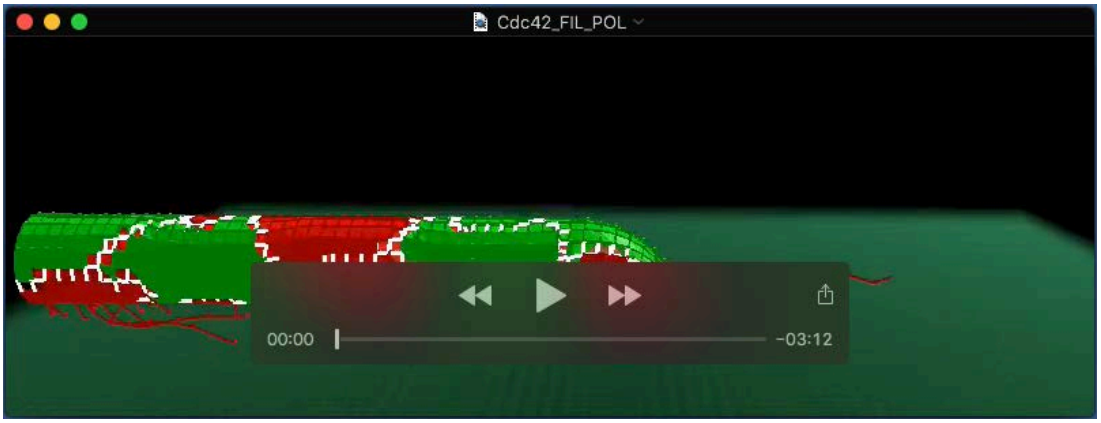

Movie 23: $Cdc42_{FIL/POL}$:WT sprout

Simulation movie showing a 1:1 $Cdc42_{FIL/POL}$:WT sprout in which the green and red cells respectively depict $Cdc42_{FIL/POL}$ and WT cells. The green $Cdc42_{FIL/POL}$ cells extend less filopodia, are less polarized and are less competent to occupy the tip position than the red WT cells. The $Cdc42_{FIL/POL}$ and WT cells both segregate vertically and horizontally. The green layer underneath the vessel shows the VEGF gradient, which linearly increases towards the tip.

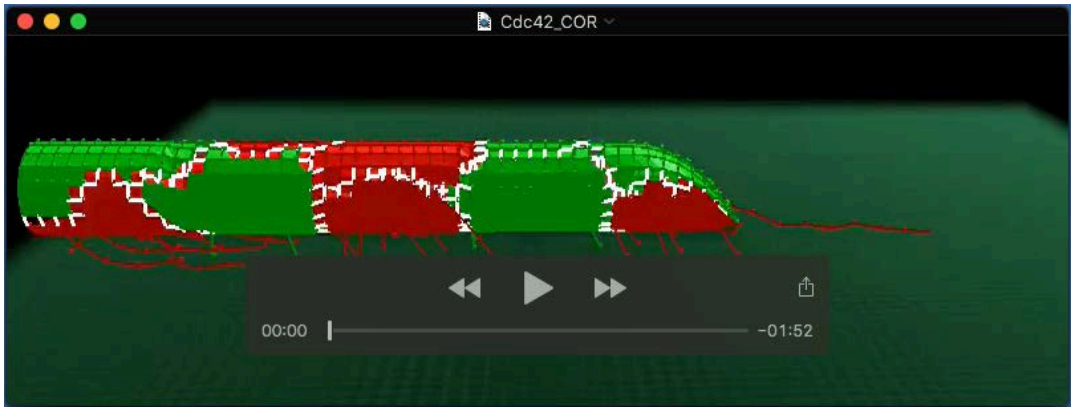

Movie 24: $Cdc42_{COR}$:WT sprout

Simulation movie showing a 1:1 $Cdc42_{COR}$:WT sprout in which the green and red cells respectively depict $Cdc42_{COR}$ and WT cells. The green $Cdc42_{COR}$ cells extend less cortical protrusions and are less competent to occupy the tip position than the red WT cells. The $Cdc42_{COR}$ and WT cells thus segregate horizontally but not vertically. The green layer underneath the vessel shows the VEGF gradient, which linearly increases towards the tip.

Movie 25: $Cdc42_{ADH}$:WT sprout

Simulation movie showing a 1:1 $Cdc42_{ADH}$:WT sprout in which the green and red cells respectively depict $Cdc42_{ADH}$ and WT cells. The green $Cdc42_{ADH}$ cells are more strongly adhesive and consequently less motile which renders them less able to occupy the tip position than the red WT cells. The $Cdc42_{ADH}$ and WT cells thus segregate horizontally but not vertically. The green layer underneath the vessel shows the VEGF gradient, which linearly increases towards the tip.

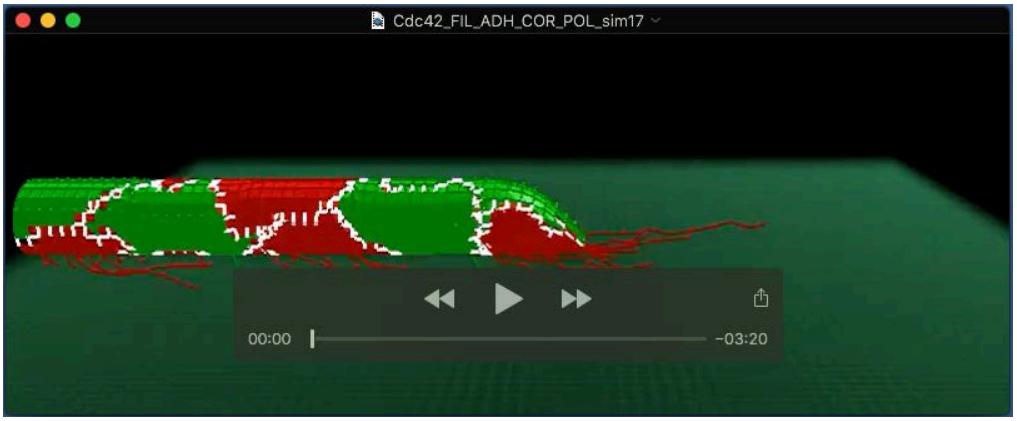

Movie 26: $Cdc42_{FIL/ADH/COR/POL}$:WT sprout

Simulation movie showing a 1:1 $Cdc42_{FIL/ADH/COR/POL}$:WT sprout in which the green and red cells respectively depict $Cdc42_{FIL/ADH/COR/POL}$ and WT cells. The green $Cdc42_{FIL/ADH/COR/POL}$ are less competent to occupy the tip position than the red WT cells. The $Cdc42_{FIL/ADH/COR/POL}$ and WT cells segregate both horizontally and vertically. The green layer underneath the vessel shows the VEGF gradient, which linearly increases towards the tip.